HHS Public Access

Author manuscript

Cell Stem Cell. Author manuscript; available in PMC 2023 June 02.

Published in final edited form as:

Cell Stem Cell. 2022 June 02; 29(6): 933–947.e6. doi:10.1016/j.stem.2022.04.016.

An injury-responsive Rac-to-Rho GTPase switch drives activation of muscle stem cells through rapid cytoskeletal remodeling

Allison P. Kann[1,2,3], **Margaret Hung**[1,2,3], **Wei Wang**[1,2,4], **Jo Nguyen**[5,6], **Penney M. Gilbert**[5,6,7], **Zhuhao Wu**[1,2,4], **Robert S. Krauss**[1,2,3,8,**]

[1]Department of Cell, Developmental, and Regenerative Biology, Icahn School of Medicine at Mount Sinai, New York, NY 10029, USA

[2]Black Family Stem Cell Institute, Icahn School of Medicine at Mount Sinai, New York, NY 10029, USA

[3]Graduate School of Biomedical Sciences, Icahn School of Medicine at Mount Sinai, New York, NY 10029, USA

[4]Department of Neuroscience, Icahn School of Medicine at Mount Sinai, New York, NY 10029, USA

[5]Institute of Biomedical Engineering, Toronto, ON M5S3G9, Canada

[6]Donnelly Centre for Cellular and Biomolecular Research, Toronto, ON M5S3E1, Canada

[7]Department of Cell and Systems Biology, University of Toronto, Toronto, ON M5S3G5, Canada

[8]Lead contact

SUMMARY

Many tissues harbor quiescent stem cells that are activated upon injury, subsequently proliferating and differentiating to repair tissue damage. Mechanisms by which stem cells sense injury and transition from quiescence to activation, however, remain largely unknown. Resident skeletal muscle stem cells (MuSCs) are essential orchestrators of muscle regeneration and repair. Here, with a combination of *in vivo* and *ex vivo* approaches, we show that quiescent MuSCs have elaborate, Rac GTPase-promoted cytoplasmic projections that respond to injury via upregulation

CORRESPONDING AUTHOR: Correspondence to Robert S. Krauss. Correspondence: Department of Cell, Developmental, and Regenerative Biology, Icahn School of Medicine at Mount Sinai, One Gustave L. Levy Place, Box 1020, New York, NY 10029, Tel: 212-241-2177, Fax: 212-860-9279, Robert.Krauss@mssm.edu.

AUTHOR CONTRIBUTIONS

Conceptualization, A.P.K. and R.S.K.; Methodology, A.P.K. and R.S.K.; Validation and Formal Analysis, A.P.K.; Investigation, A.P.K., M.H., W.W., and J.N.; Writing – Original Draft, A.P.K. and R.S.K.; Writing – Review & Editing, A.P.K. and R.S.K.; Visualization, A.P.K.; Supervision, R.S.K., Z.W., and P.M.G.; Funding Acquisition, A.P.K., R.S.K., M.H., J.N., and P.M.G. All authors approved the final manuscript.

DECLARATION OF INTEREST

The authors declare no competing or financial interests.

of Rho/ROCK signaling, facilitating projection retraction and driving downstream activation events. These early events involve rapid cytoskeletal rearrangements and occur independently of exogenous growth factors. This mechanism is conserved across a broad range of MuSC activation models, including injury, disease, and genetic loss of quiescence. Our results redefine MuSC activation and present a central mechanism by which quiescent stem cells initiate responses to injury.

Graphical Abstract

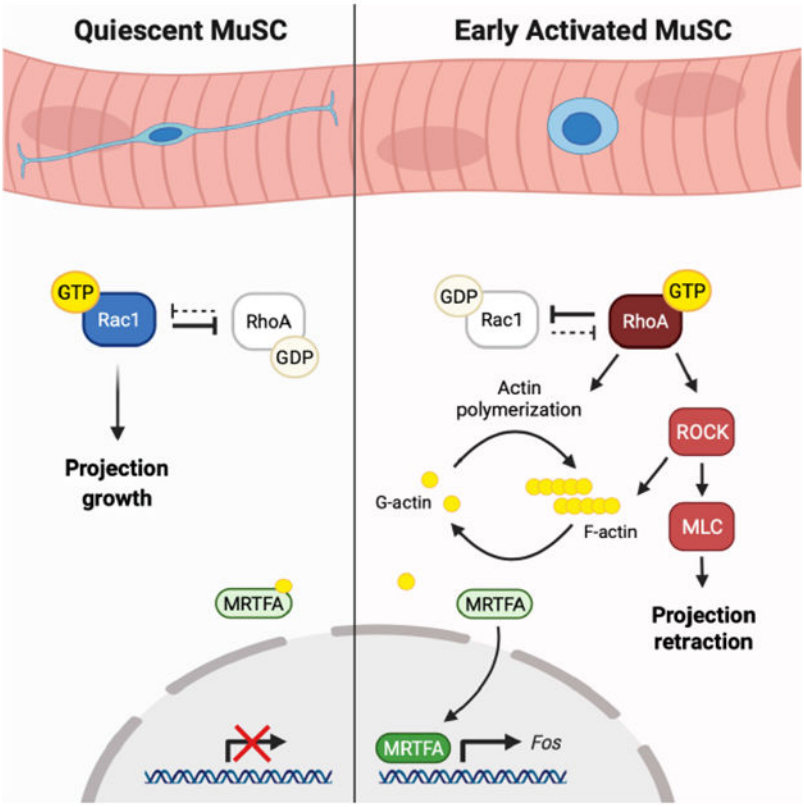

eTOC blurb:

Quiescent muscle stem cells (MuSCs) have long, elaborate, cytoplasmic projections *in vivo*. In this manuscript, Kann and colleagues identify a mechanism by which MuSCs break quiescence through a small GTPase activity switch, driving projection retraction, cytoskeletal rearrangements, and downstream events important for stem cell activation.

INTRODUCTION

Muscle stem cells (MuSCs) are the adult stem cell population found in skeletal muscle, responsible for facilitating tissue regeneration. MuSCs are maintained in a quiescent state during homeostasis, but upon injury they activate, proliferate, and differentiate to form new muscle (Brack and Rando, 2012; Yin et al., 2013). While many factors that regulate the quiescence-to-activation (Q-A) transition have been identified, the events that initiate this

process remain unknown. Quiescent MuSCs are polarized, adhering to myofibers through cadherins (Goel et al., 2017; Hollnagel et al., 2002) and a basal lamina through integrins (Rozo et al., 2016). Both genetic and physical perturbation of niche adhesion induces a loss of quiescence (Goel et al., 2017; Rozo et al., 2016), suggesting that changes in cytoskeletal dynamics may be involved in initiation of the Q-A transition. Identification of these very early cellular and physical cues, however, has been limited by the mechanosensitivity of MuSCs. Dissociation and isolation of MuSCs leads to activation, evidenced by significant transcriptomic differences between *in vivo* MuSCs and their isolated counterparts (Machado et al., 2017; van den Brink et al., 2017; van Velthoven et al., 2017; Yue et al., 2020). This phenomenon is linked to a stress response during isolation but is conserved across mechanisms of MuSC activation, with few differences between isolation- and injury-induced activation (Almada et al., 2021; Machado et al., 2021).

In addition to changes in transcription, dissociation of MuSCs stimulates changes in cell shape. MuSCs *in vivo* have long cytoplasmic projections, most of which are lost during *ex vivo* isolation (Verma et al., 2018). Changes in cell shape and structure are often driven by the Rho family of GTPases (Rho, Rac, and Cdc42), membrane-bound small GTP-binding proteins that mediate cytoskeletal rearrangements, downstream signaling, and transcriptional changes in response to extracellular cues (Burridge and Wennerberg, 2004). Rac and Cdc42 have distinct functions but share some downstream effector proteins, whereas Rho acts upon its own set of effectors. While feedback mechanisms are present between all three GTPases, an inverse relationship exists between Rac and Rho that often functions as a molecular switch, coordinating changes in cell morphology, migration, and proliferation (Guilluy et al., 2011). Despite their significance across cell types, Rho GTPases have not been extensively studied in MuSC biology. RhoA was identified as a downstream effector of myofiber-derived Wnt4 signaling, critical in maintaining quiescence (Eliazer et al., 2019). Rac1 has been implicated in later stages of regeneration (Bentzinger et al., 2014), with no known role in MuSC quiescence.

In this report, we combine *in vivo* tissue clearing with a modified *ex vivo* single myofiber preparation to gain an unprecedented look at the quiescent MuSC. Using these systems, we have identified a function for Rac1 in quiescence and a mechanism by which quiescent MuSCs respond to injury via a Rac-to-Rho GTPase switch, facilitating retraction of cytoplasmic projections and initiating downstream signaling events to drive early activation.

RESULTS

Quiescent MuSCs have long, elaborate projections that can be maintained *ex vivo*

For decades, quiescent MuSCs have been described as fusiform cells with high nuclear-to-cytoplasmic ratio (Muir, 1965; Yin et al., 2013). Some older and recent imaging studies, however, revealed that MuSCs possess cytoplasmic projections *in vivo* (Haroon et al., 2021; Schmalbruch, 1978; Verma et al., 2018; Webster et al., 2016). Little is known of these structures, as they are lost upon MuSC isolation, preventing any high-resolution characterization. Using a tamoxifen-inducible strategy to label adult MuSCs (with $Pax7^{CreERT2};R26^{LSL\text{-}tdT}$ mice) followed by tissue clearing (Chi et al., 2018), we confirmed that quiescent MuSCs possess heterogeneous morphologies with long, complex projections

(here termed quiescent projections, QPs) (Fig. 1A). These QPs often displayed multiple branches and filopodia (Fig. 1B). We observed no significant differences in QP length or complexity across regions of hindlimb muscle (Fig. S1A–F). MuSCs in the forelimb (a population containing a higher percentage of Pax3+/Pax7+ cells than the hindlimb (Der Vartanian et al., 2019)), however, showed slightly longer QPs and higher complexity than their counterparts in the hindlimb. They were also more frequently aligned with the perpendicular axis of their resident myofibers, whereas MuSCs in the hindlimb were primarily parallel (Fig. S1A–F).

To better characterize these structures, we isolated primary single myofibers, an *ex vivo* technique that maintains MuSCs in their immediate niche (Fig. 1C). QPs are lost during traditional preparation of myofibers, but modifications to this protocol (see Methods) enabled maintenance of these structures. Critical to this achievement was minimization of muscle stretch during preparation. When fixed immediately after isolation (T0), MuSCs on these preparations had QPs resembling those seen *in vivo* (Fig. 1D). Our modified protocol maintains higher percentages of cells with QPs than the standard technique, though comparison to *in vivo* numbers reveals that most QPs still partially or fully retracted during preparation (Fig. 1E–F). In addition to the difference in QP lengths, retraction can be detected through the following observations: 1) MuSCs and myofibers adhere to one another via cadherin-based adherens junctions (AJs) (Goel et al, 2017), and puncta of AJ components were present on myofibers at sites where MuSCs had recently been in direct contact with them (Fig. S1G); and 2) grooves in the sarcolemma marking sites of QP occupation were observed by immunolabeling the myofiber surface (Fig. 1G). This latter approach also showed that after QP retraction, MuSC cell bodies continued to contract beyond their original surface area of myofiber contact.

Changes in cell shape and retraction of cytoplasmic extensions is a process driven by cytoskeletal rearrangements (Dogterom and Koenderink, 2019). Immunofluorescence staining for cytoskeletal elements revealed a prominent microtubule (MT) network within MuSCs, with dense localization of α-tubulin within QPs (Fig. 1H). Visualization of F-actin in MuSCs is challenging due to intense signal from sarcomeres within adjacent myofibers. Occasionally, however, MuSCs in these preparations partially dissociated from their myofibers, revealing that the central MT core within QPs is surrounded by cortical F-actin (Fig. 1I). Although the majority of filopodia seen in cleared tissue are lost upon myofiber dissociation, some remaining tips of QPs were enriched for the actin-binding protein Arp3, a known pro-migratory factor in other cell projections (Korobova and Svitkina, 2008) (Fig. 1J–K). The cell adhesion molecule N-cadherin (Ncad) promotes MuSC quiescence (Goel et al., 2017) and is a regulator of the cytoskeleton and cell motility (De Wever et al., 2004; Jossin and Cooper, 2011). Strikingly, Ncad signal was often detected within QPs *ex vivo* and *in vivo*, frequently enriched at their tips (Fig. 1L–M, Fig. S1H). This localization was not shared by other AJ components, including additional cadherins and catenins, all of which were detected throughout the apical membrane regardless of projection status (Fig. S1I). Upon QP retraction, Ncad redistributed along the apical membrane to the body of the MuSC (Fig S1J).

Collectively, these data characterize quiescent structures within MuSCs previously inaccessible to high-resolution microscopy. QPs contain a MT-dense network and share characteristics of motile cellular structures found in other cell types (Bernier et al., 2019), suggesting an active role for cytoskeletal dynamics in MuSC quiescence.

Retraction of projections is an early MuSC activation response

The loss of projections upon isolation implies that projection retraction is an early response to niche perturbation. To test whether QPs retract *in vivo*, we performed a focal needle puncture injury on extensor digitorum longus (EDL) muscle, followed by perfusion and tissue clearing. Within three hours after injury, MuSCs around the site of puncture had retracted their QPs, confirming this as a very early injury response (Fig. 2A). This retraction was not observed throughout the entire muscle, suggesting that projections are sensing and responding to local injury stimuli. Injury of the TA muscle with barium chloride ($BaCl_2$) was sufficient to stimulate partial (but not full) retraction of projections in nearby EDLs two hours post-injury (Fig. S2A–C), the partial response likely due to a delay in exposure of the EDL to the chemical.

We next turned to our modified myofiber protocol to study intracellular events associated with QP retraction. Typically used to study the Q-A transition, myofibers can be cultured in the presence of exogenous growth factors (GF), which induce changes thought to mimic *in vivo* MuSC activation (Pasut et al., 2013). We cultured myofibers with GF for short time courses *ex vivo* and observed significant morphological changes in MuSCs (Fig. 2B). Approximately 90% of MuSCs lost their QPs within one hour, and they subsequently developed shorter, more ramified protrusions, an “activated morphology” previously linked to myogenic progenitor migration after injury (Webster et al., 2016) (Fig. 2C). The addition of $BaCl_2$ to myofibers *ex vivo* rapidly accelerated the loss of QPs (Fig. S2D), further validating a link between QP retraction and response to injury stimuli.

Because QPs began retracting prior to the addition of exogenous GF, we speculated that added GF may be unnecessary for these initial events. We cultured myofibers in the presence and absence of GF and observed no changes in the rate of QP retraction (Fig. 2C). The myofiber itself may act as a source of GF (Chakkalakal et al., 2012), making it impossible to fully rule out a role for GF signaling from the immediate niche in these earliest events. Interestingly, however, the later shift from a rounded to an activated morphology within 4 hours was dependent on the addition of exogenous GF (Fig. 2C). This suggests a temporal shift in activation, from early events that can be induced solely by the immediate niche towards those reliant on exogenous GF.

To determine if projection retraction was associated with other signs of activation, we compared T0 MuSCs ± QPs for two known, early signs of the Q-A transition: dissociation of Ddx6+ mRNP granules, which sequester *Myf5* transcripts during quiescence (Crist et al., 2012), and cellular/nuclear rounding caused by a loss of tension (Eliazer et al., 2019). MuSCs with QPs had higher numbers of Ddx6+ granules and more ovoid nuclei than those without projections, indicating that QP retraction correlates with initiation of these early events (Fig. S2E–H). In addition to these known signs of activation, immunofluorescence for α-tubulin revealed significant differences in MT organization between cells ± QPs (Fig. 1I,

Fig. 2D), likely a consequence of retraction-associated MT dynamics. Reorganization of the MT cytoskeleton was visualized by the formation of a γ-tubulin+/pericentrin+ centrosomal microtubule organizing center (cMTOC) (Fig. 2D, Fig. S2I). The cMTOC was always positioned at a site of nuclear indentation, and formation of this indentation marked the initiation of complex nuclear shape rearrangements that accompanied nuclear rounding early in the Q-A transition (visualized with immunofluorescence for Lamin B1, Fig. S2G). While all MuSCs without QPs were cMTOC+, 58% of MuSCs with QPs had also undergone this MT reorganization (Fig. 2E). All MuSCs were cMTOC+ by 1 hour after isolation. To confirm that cMTOC formation is an event that also occurs in response to injury *in vivo*, we compared MT organization in MuSCs within perfusion-fixed myofiber bundles from control and early-injured (3 hours post-$BaCl_2$ injury, 3hpi) mice. Similar to our *ex vivo* results, the few MuSCs in control muscle without QPs were all cMTOC+ (Fig. 2F–G). Of the ~85% of MuSCs with QPs in control muscle, the great majority lacked a cMTOC. In contrast, the majority of MuSCs at 3hpi were cMTOC+ (Fig. 2F–G). cMTOC formation is therefore a very early activation response, occurring during projection retraction.

These results demonstrate that retraction of QPs is an early activation event, occurring in response to injury and isolation. MuSCs with QPs display features of “deeper” quiescence than MuSCs without them, and MT reorganization is a clear indicator of activation that occurs during QP retraction.

Rac activity is high in quiescent MuSCs and downregulated upon activation

Rho family GTPases are key regulators of the cytoskeleton, and crosstalk between GTPases facilitates dynamic extension and contraction of projections in many cell types (Dupraz et al., 2019; Kalpachidou et al., 2019). Long cytoplasmic projections and filopodia like those seen in quiescent MuSCs are typically associated with high levels of Rac/Cdc42 activity, which function in concert to promote protrusion outgrowth. To assess whether loss of QPs is associated with downregulation of GTPase activity, we used an *in situ* binding assay for active Rac/Cdc42 and performed a short *ex vivo* time course on myofibers. At T0, MuSCs with QPs had higher Rac/Cdc42 activity than those without QPs, and there was a downward trend in activity in all cells between T0-T4 (Fig. 3A–C). This indicates that Rac/Cdc42 activity was high in quiescent cells, then quickly reduced as MuSCs entered early activation. Immunofluorescence staining revealed enrichment of Rac1 protein in the tips of T0 QPs and a similar downregulation of total Rac1 levels by T4, suggesting that regulation of Rac1 protein levels is a major component of this activity (Fig. S3A).

Isolation of myofibers in the presence of the Rac-specific inhibitor NSC23766 (NSC) (Fig. 3D) decreased levels of active Rac (Fig. S3B) and accelerated the earliest signs of activation. Retraction of QPs and cMTOC formation were more prominent at T0 in NSC-treated cells than control cells (Fig. 3E–H, Fig. S3C). Furthermore, Rac inhibition increased the percentage of T0 cells expressing FOS, an early transcriptional event in MuSC activation, and which plays a key role in the early regenerative program (Fig. 3I) (Almada et al., 2021). FOS is induced rapidly, and within one hour (T1) the number of FOS+ MuSCs was similar between control and NSC conditions. At T4, NSC treatment did not affect the percentage of MuSCs expressing the myogenic transcription factor and activated MuSC marker, MYOD

(Fig. S3D). These data fit a model in which Rac activity is high in quiescent MuSCs, then quickly downregulated during the Q-A transition. Small molecule inhibition of Rac accelerated the very earliest steps, but continued inhibition had no effect on subsequent activation events.

We next conditionally removed *Rac1* from adult MuSCs to test the function of Rac1 in MuSC quiescence *in vivo* (Fig. 3J). The effects of certain key regulators of MuSC biology are dosage sensitive (de Morree et al., 2017; Eliazer et al., 2019), and we therefore examined the effects of *Rac1* haploinsufficiency alongside complete genetic removal. We observed a dosage-dependent break in homeostatic quiescence, detected through an increase in the percentage of MuSCs expressing the activation markers MYOD and Ki67, as well as an increase in interstitial MuSCs (Fig. 3K–O). Consistent with this phenotype, $Rac1^{fl/+}$ and $Rac1^{fl/fl}$ MuSCs displayed fewer and shorter QPs than control cells (Fig. S3E–H), and percentages of MYOD+ MuSCs at T0 on myofibers followed the same trend seen *in vivo* (Fig. S3I). Full removal of Rac1 from MuSCs resulted in a significant reduction in MuSC numbers *in vivo*, whereas heterozygous mice showed no change (Fig. 3P). Taken together, these data demonstrate that Rac1 is necessary for maintenance of QPs and MuSC quiescence, and MuSCs transition from a Rac^{high} to Rac^{low} activity state during the Q-A transition.

The Rho/ROCK/MLC pathway mediates projection retraction and early activation

While Rac generally promotes outgrowth of cellular projections, Rho GTPase drives actomyosin contractility and retraction (Dupraz et al., 2019). We hypothesized that quiescent Rac^{high} MuSCs may respond to injury through a GTPase switch, upregulating Rho activity to facilitate QP retraction and downstream activation events. Using an *in situ* binding assay for active Rho, we observed that Rho activity followed the opposite trend as that of Rac, increasing as MuSCs retracted their projections, then further increasing between T0-T4 (Fig. 4A–C). Despite the lack of requirement for exogenous GF in QP retraction, the increase in Rho activity post-retraction was dependent upon the addition of GF (Fig. 4C). The highest levels of active Rho (seen at T4) correlated with acquisition of the activated MuSC morphology seen in these cells at this time point (Fig. 2B–C), which also required GF addition. These results imply there is a role for exogenous ligands in regulating MuSC shape during early activation, after QP retraction.

Rho kinase (ROCK) is a downstream effector of Rho that signals through myosin light chain (MLC) to facilitate actomyosin contractility (Kimura et al., 1996). The QP retraction and cell contractility observed in response to injury and isolation implicated ROCK/MLC signaling as an early component of activation. To test this hypothesis, myofibers were cultured with Rho/ROCK/MLC pathway inhibitors (Fig. 4D). Isolation of myofibers in the presence of the MLC inhibitor Blebbistatin, which prevents cell contractility, yielded higher average QP percentages and lengths than control myofibers at T0 (Fig. S4A–D). However, prolonged culture in Blebbistatin led to MuSC detachment and loss from myofibers, preventing extensive analysis at later time points (Fig. S4E).

Strikingly, isolation of myofibers in the presence of the ROCK inhibitor Y-27632 (Y27) preserved quiescent MuSC morphology (Fig. 4E). At T0, Y27-treated preparations had a

percentage of MuSCs with QPs and projection lengths similar to MuSCs *in vivo* (Fig. 4F–G, Fig. S4D). Y27-treated MuSCs displayed filopodia and Arp3 enrichment at the ends of their QPs, features that are normally lost during isolation (Fig. 4H, Fig. S4F). Loss of quiescent structures is therefore driven by Rho/ROCK/MLC-mediated retraction. To assess whether Rho/ROCK signaling is required for the Q-A transition, we cultured myofibers in Y27 for various times. Early activation events such as cMTOC formation (T0) and FOS induction (T0-T2) were diminished in response to Y27 treatment (Fig. S4G, Fig. 4I). Levels of MYOD expression were similarly reduced (T4-T8, Fig. 4J, Fig. S4H), and S-phase entry was delayed (T30, Fig. 4K), confirming the significance of ROCK signaling in MuSC activation.

Rho and Rac GTPases frequently function in a mutually inhibitory equilibrium, and inhibition of ROCK has been shown to hyperactivate Rac and diminish Rho activity (El-Sibai et al., 2008; Priya et al., 2015). Y27-treated MuSCs had low levels of active Rho and maintained both high levels of Rac activity and total Rac1 protein throughout a time course (Fig. S4I–L). By four hours in Y27, QPs took on a highly elaborated morphology that resembled MuSCs with the most complex projections *in vivo* (Fig. S4M). These data support our earlier findings on the role of Rac1 in quiescence and further link high levels of Rac activity to the maintenance and elongation of quiescent MuSC structures.

In vitro culture of MuSCs remains a significant hurdle in the field, and maintenance/restoration of quiescent characteristics to purified MuSCs has proved challenging (Gilbert et al., 2010; Quarta et al., 2016). We asked whether ROCK inhibition was sufficient to induce formation of QPs in cells that had already undergone early activation. Isolated MuSCs were plated at single cell density on laminin-functionalized polyacrylamide hydrogels (Lutolf et al., 2009). While untreated cells consistently took on a morphology resembling activated SCs, inclusion of Y27 for ~24 hours induced a morphology resembling *in vivo* quiescent SCs, and many acquired projection lengths similar to QPs (Fig. 4L–M). Collectively, these data identify Rho/ROCK/MLC signaling as a driver of early activation events and suggest GTPase dynamics may be targeted in restoration of quiescent properties to MuSCs *in vitro*.

Rho signaling initiates *Fos* induction in the Q-A transition

To determine whether this Rac-to-Rho GTPase switch is functionally linked to transcriptional events during early activation, we took a closer look at the regulation of FOS. *Fos* transcription occurs in response to muscle injury and as a consequence of enzymatic dissociation of MuSCs from bulk tissue (Machado et al., 2021), but the mechanisms underlying this event are unknown. Modulation of Rac or Rho activity affected FOS levels at early time points, suggesting that this GTPase switch affects FOS induction directly or indirectly.

The *Fos* promoter contains multiple enhancers, including both a calcium/cAMP-responsive element (CaCRE) and a serum response element (SRE). *Fos* can therefore be induced by multiple signaling events, including elevation of intracellular cAMP and/or Ca2+, Ras/RAF/MEK/ERK-dependent signaling, and Rho-dependent cytoskeletal signaling (Fig. 5A) (Bar-Sagi, 2000; Sheng and Greenberg, 1990). We found that T0 MuSCs with QPs were uniformly FOS-, whereas ~40% of MuSCs without QPs were FOS+ (Fig. 5B–C). By T1,

~80% of all MuSCs were FOS+ (Fig. 5D). We compared the percentage of FOS+ cells in myofibers cultured in the presence or absence of GF and saw no difference until T4. At this time point, GF maintained a high percentage of FOS+ cells, whereas this began to fall off in the absence of GF (Fig. 5D). FOS induction therefore occurs after QP retraction, potentially in response to Rho-dependent cytoskeletal rearrangements.

To investigate the role of Rho signaling in regulating FOS, we focused on the protein MRTFA. MRTFA (also called MAL1/MKL1) rapidly translocates from the cytoplasm to the nucleus to drive SRF activation in response to Rho-dependent actin cytoskeleton rearrangements (Cen et al., 2004; Miralles, 2003). We found that MRTFA was present in the nucleus of all T0 MuSCs (Fig. 5E–F). Contrary to a previous report (Randrianarison-Huetz et al., 2018), we found that all T0 MuSC nuclei were positive for SRF (Fig. S5A). Y27 treatment caused a small but significant decrease in MuSCs with nuclear MRTFA, suggesting that this translocation is at least partially induced by Rho/ROCK signaling during isolation (Fig. 5F). Immunofluorescence on both cross-sections of TA muscle and whole-mount perfusion-fixed EDL muscle revealed that MuSCs in uninjured muscle *in vivo* lacked nuclear MRTFA signal (Fig. 5G, Fig. S5B). MRTFA was observed in the majority of MuSC nuclei early after $BaCl_2$ injury (1.5 hpi) (Fig 5G–H), confirming MRTFA nuclear translocation as an extremely early event in the Q-A transition.

We next looked at the relationship between MRTFA and FOS. All MRTFA+ cells *in vivo* also expressed FOS, with numbers of double-positive cells increasing dramatically by 1.5 hpi (Fig. S5C–D). Myofibers isolated in the presence of CCG-203971 (CCG), a Rho/MRTFA/SRF pathway inhibitor that interferes with nuclear localization and function of MRTFA (Hutchings et al., 2017), showed a significant reduction in nuclear MRTFA accumulation (Fig. 5F, Fig. S5E). CCG treatment prevented FOS induction at T0, confirming a role for MRTFA in the initiation of this step (Fig. 5I). By T1, however, moderate percentages of FOS+ cells were observed despite MRTFA inhibition, suggesting a role for additional or compensatory mechanisms in driving FOS levels. These results are consistent with the effects of GTPase inhibition on FOS levels; the earliest wave of FOS is dependent on Rho/MRTFA signaling, and manipulation of GTPase dynamics showed the most significant effects on FOS levels at T0.

Continued CCG treatment had no effect on MuSC activation at early (T4 MYOD levels, Fig. S5F) or late (T30 EdU incorporation, Fig. S5G) time points, consistent with previous findings that SRF is not essential for MuSC activation (Randrianarison-Huetz et al., 2018). Isolation of myofibers in the presence of the MEK inhibitor PD98059 (PD), which targets multiple downstream pathways (including TCF/SRF and some mechanisms of CaCRE usage), had no effect on nuclear MRTFA accumulation or FOS induction at T0, but yielded a similar degree of inhibition of FOS induction at T1-T2 as the CCG-treated cells (Fig. 5F, 5I). Treatment of MuSCs with both CCG and PD prevented FOS induction entirely (Fig. 5I).

FOS induction, one of the earliest known transcriptional indicators of MuSC activation, is therefore initiated by Rho/MRTFA signaling. MEK-dependent mechanisms join shortly afterward to coordinate a rapid and robust FOS response, FOS in turn contributing to the early activation of MuSCs.

Projection dynamics are a general feature of MuSC activation

To determine if these cellular dynamics are broadly conserved *in vivo*, we used tissue clearing to test various models of MuSC activation. SC-specific deletion of Ncad promotes the Q-A transition in the absence of injury and inflammation (Goel et al., 2017), and Ncad is enriched within QPs. We therefore hypothesized that Ncad promotes outgrowth and/or maintenance of QPs, its loss facilitating the early events downstream of projection retraction. Genetic removal of Ncad from adult MuSCs resulted in a substantial reduction *in vivo* of both the percentage of MuSCs with QPs and the length of the remaining QPs as compared to controls (Fig. 6A–B,F–G), linking a phenotypic break in quiescence with projection loss *in vivo*.

We next turned to the well-characterized *mdx* mouse model of muscular dystrophy. The muscles of these animals undergo cycles of degeneration and MuSC-mediated regeneration (Sacco et al., 2010). We found that ~90% of MuSCs in *mdx* muscles presented an activated morphology (Fig. 6C,F). We observed a similar phenomenon in the context of $BaCl_2$ injury. While injury of the TA caused partial retraction of QPs at 2hpi (Fig. S2A–C), at two days post-injury (2dpi), ~90% of EDL MuSCs in the injured leg had adopted an activated morphology (Fig. 6D,F). MuSCs in the contralateral leg of 2dpi mice enter a state termed G_{alert}, in which they are primed for more rapid activation than control MuSCs (Rodgers et al., 2014). Strikingly, G_{alert} MuSCs had shorter projections than MuSCs in uninjured muscles (Fig. 6E–G). These findings demonstrate that retraction and/or shortening of projections is a general property of the Q-A transition irrespective of the means of activation, whether via genetic removal of quiescence-promoting niche factors, muscle disease, or muscle injury.

DISCUSSION

Mechanisms whereby quiescent stem cells sense and respond to tissue damage are a persistent enigma in regenerative biology. While cellular responses to injury have been examined in other tissue systems (Aragona et al., 2020; Niethammer, 2016), there is little evidence to link changes in single-cell contractility and morphology to downstream molecular events in MuSCs. Here we present a mechanism by which quiescent MuSCs respond to injury and break quiescence through a Rac-to-Rho GTPase switch. Rac activity is high in quiescent MuSCs, promoting QP outgrowth and/or maintenance and preventing MuSC activation. Rac signaling is downregulated in the earliest steps of activation, and an increase in Rho/ROCK signaling is required for retraction of QPs and timely entry into the Q-A transition.

Cell protrusions are present in most cells, but the concept of cell projections as mediators of stem cell behavior has been primarily studied in invertebrate systems (Buszczak et al., 2016). Niche cells use projections to physically enwrap and signal to stem cells (Linden et al., 2017), and recent work has also identified protrusions within neural, intestinal, and germline stem cells in *Drosophila* (Endow et al., 2019; Inaba et al., 2015). To date, MuSCs are the only mammalian stem cell type with discernable projections *in vivo*. Interestingly, however, the expression of *Lgr4/5* (known markers for many stem cells) can induce

cytoneme-like structures in cultured cells (Snyder et al., 2015), suggesting that projections might exist in other stem cell systems.

Our findings present the notion that rearrangement of the MuSC cytoskeleton and loss of QPs is among the earliest events in the Q-A transition. Induction of *Fos* is one of the earliest known transcriptional events in MuSC activation (Almada et al., 2021; Machado et al., 2021); we find that retraction of QPs occurs upstream of FOS detection. Even prior to full QP retraction, we observe the formation of a cMTOC and nuclear translocation of the transcription factor MRTFA, events mediated by rearrangement of the MT and actin cytoskeletons, respectively. Both cMTOC formation and MRTFA translocation were promoted by the Rac-to-Rho activity switch and affected by GTPase inhibition. Furthermore, each began to occur during muscle isolation and were evident in most or all MuSCs by T0. One of the most important steps in maintaining QPs *ex vivo* was the minimization of mechanostimulation during excision and myofiber preparation, suggesting that at least some of the initial signals driving the Q-A transition are biomechanical in nature. Consistent with this likelihood, nuclear translocation of MRTFA is a known mechanoresponsive signal (Reed et al., 2021). QP retraction, cMTOC formation, MRTFA translocation, and *Fos* induction all occurred without addition of exogenous GF generally provided to myofiber preparations. It is probable that the presence of exogenous GF in *ex vivo* preparations promotes a maximal activation response, but they were not necessary for these earliest events to occur. It is, however, possible that isolated myofibers provide GF to their associated MuSCs, as inhibition of MEK (which is often activated by GF) along with MRTFA inhibition completely blocked *Fos* induction *ex vivo.* Furthermore, the p38α/β MAP kinase pathway, which can be triggered by a variety of extracellular stimuli, is also activated extremely rapidly upon MuSC activation to drive initial signaling events that promote this process (Hausburg et al., 2015). Biomechanical, GF-dependent, and other signals may therefore occur in tightly overlapping time frames during the Q-A transition.

The bodies of MuSCs are stationary during quiescence (Baghdadi et al., 2018), but QPs have features in common with migrating neuronal projections and are likely dynamic *in vivo*. The concept of cytoplasmic cellular projections as sensors of their environment has been associated with microglia, in which resting microglia sense tissue damage through their elaborate protrusions (Bernier et al., 2019; Prinz et al., 2019), but no such surveillance mechanism has been reported in stem cells. We hypothesize that MuSCs are in a dynamic state during homeostasis in which projections are motile structures, probing the surface of their immediate niche for myofiber damage and/or its sequelae, then responding with complete retraction to fully enter the Q-A transition. The preservation of projections appears vital for the maintenance of quiescence; depletion of Ncad or Rac1 (both known regulators of projection outgrowth (Jossin and Cooper, 2011)) in MuSCs leads to both a reduction in QP number/length and a propensity of MuSCs to enter the Q-A transition in the absence of injury.

Remarkably little is known about the function of Rho GTPases in MuSCs. RhoA has previously been identified as a promoter of MuSC quiescence, working downstream of myofiber-derived Wnt4 to prevent MuSC activation (Eliazer et al., 2019). Superficially, this phenotype seems incompatible with our data demonstrating the significance of Rho/ROCK

signaling in the Q-A transition. However, there are multiple potential ways in which our results can be reconciled with this observation. First, RhoA is important in cell adhesion (Fukata and Kaibuchi, 2001), and many *RhoA*$^{+/-}$ MuSCs were located outside the basal lamina, thus depriving them of myofiber-provided adhesion necessary for maintenance of quiescence (Goel et al., 2017). It is also possible that different members of the Rho family play functionally distinct roles in MuSC biology. The Rho signaling described in this report may be driven by RhoC, for example, whose expression is enhanced during early activation (Liu et al., 2013; Machado et al., 2017). Additionally, our hypothesis that QPs serve as dynamic regulators of quiescence implies a cross-regulated equilibrium between Rac1 and Rho activities. MuSC quiescence relies on Rac1 (and possibly Cdc42) activity for outgrowth of projections, but those projections must partially or fully retract to maintain a homeostatic system and properly survey their environment. This equilibrium must therefore include some basal level of localized Rho activity during quiescence to facilitate reversible retraction. The strong phenotypic similarity of *Rac1* and *RhoA* heterozygous mice – including expression of MuSC activation markers and an increase in interstitial MuSCs in the absence of injury – suggests that perturbation of this dynamic system in either direction may induce a propensity to break quiescence.

Both genetic and small molecule inhibitor approaches demonstrated a temporal role for Rac in which activity is high during quiescence and downregulated during the early Q-A transition. There are many potential regulators of Rac activity, including the homophilic AJs between myofiber and MuSC. Cadherin-mediated ligation has been shown to activate Rac and Cdc42 (Kim et al., 2000; Kraemer et al., 2007; Lu and Krauss, 2010), and Rac/Cdc42 have in turn been identified as positive regulators of AJs (Fukata and Kaibuchi, 2001). Given the significance of Ncad in maintaining MuSC quiescence (Goel et al., 2017) and the similarity in projection phenotype seen in Ncad mutant and Rac1 heterozygous mice (Fig. 6B), there may be signaling and feedback between these proteins during MuSC quiescence. Within MuSC biology, Rac1 has been implicated only in later stages of activation, driving myoblast motility in response to Wnt7a and fibronectin (Bentzinger et al., 2014). Later events in activation may shift the GTPase equilibrium away from Rho back towards a Rac^{high} state, enabling migratory processes needed for MuSCs to reach the site of injury. The cyclic and bimodal nature of Rho-Rac switches is becoming increasingly apparent (Byrne et al., 2016; Gould et al., 2016), and it is therefore likely that these GTPases act reiteratively, their functions shifting in response to temporal changes during activation.

Our data describe cytoskeletal events that facilitate activation in response to Rho activity, but the exact initiating event that triggers this Rac-to-Rho switch remains unknown. A diverse array of mechanisms signal to Rho, including (but not limited to) GPCRs, growth factor signaling, tension-sensitive ion channels (e.g. Piezo1, which is found in MuSCs (Hirano et al., 2021)), cell-cell adhesion, and cell-matrix adhesion (Bhadriraju et al., 2007; Provenzano and Keely, 2011). Interestingly, a very recent study reported that heterogeneity of MuSC projections was regulated during homeostasis and regeneration by Piezo1 (Ma et al., 2022), an observation consistent with this study and the notions put forth above. Rho can also be activated through calcium-dependent signaling pathways (Pardo-Pastor et al., 2018; Sakurada et al., 2003; Takemura et al., 2009), an intriguing possibility given the role of calcium dynamics in activation of neural stem cells (Gengatharan et al., 2021) and the

release of calcium from myofibers upon muscle injury (Morton et al., 2019; Wang et al., 2005). These hypotheses are not mutually exclusive. It is also possible that the mechanism by which Rho is activated might vary depending on the type of injury, with multiple potential upstream regulators facilitating a regenerative response that is flexible, rapid, and robust.

This study provides significant insights into the biology of quiescent MuSCs, identifying a mechanism by which stem cells transduce injury sensation and exit quiescence. The findings reported here open a previously unavailable window on MuSC quiescence and the Q-A transition, providing a range of possibilities for study and exploitation of muscle stem cell biology.

LIMITATIONS OF STUDY

One of the foremost challenges in studying adult stem cells is maintaining quiescence in systems which permit study of the early Q-A transition. The findings and techniques of this study expand the boundaries of our ability to visualize such events, but the mechanosensitivity of MuSCs remains a rate-limiting step (see Discussion). Even with our modified protocol, study of these early activation events is limited by the speed at which MuSCs activate upon muscle perturbation, providing only a small window during which quiescent structures can be maintained or preserved. This rapid activation prevents the use of molecular tools such as siRNAs, hence our use of small molecule inhibitors that can rapidly exert their effects on cells. This study did not incorporate intravital imaging, which has been previously used in one study to assess MuSC dynamics after injury (Webster et al., 2016), due to its inability to visualize QPs at a high resolution. We therefore used tissue clearing to image the detailed morphology of unperturbed MuSCs and used our modified myofiber preparation to assess retraction-related events. It is possible that both techniques may lead to some alterations in homeostatic MuSC morphology, due to physical perturbation or use of chemical fixative.

We used *in situ* assays to quantify small GTPase activity in MuSCs on myofibers and demonstrated that inhibitors of these factors had the predicted effects on their target's activities. Ideally, changes in GTPase activity across time points or drug conditions could also be confirmed via quantitative western blotting techniques. However, the small number of MuSCs/myofiber and the changes that occur upon dissociation of MuSCs from myofibers prevented biochemical analysis of Rac and Rho activities. Finally, our ability to visualize and analyze changes to the actin cytoskeleton was limited. While Rac and Rho GTPases almost certainly facilitate such changes during the Q-A transition, further MuSC-specific genetic labeling tools will be necessary to visualize these dynamics. These experiments will be challenging, but not impossible, and can be pursued in future studies.

STAR METHODS

RESOURCE AVAILABILITY

Lead contact—Further information and requests for resources and reagents should be directed to and will be fulfilled by the lead contact, Robert S. Krauss (robert.krauss@mssm.edu).

Materials availability—This study did not generate new unique reagents.

Data and code availability

- Data reported in this paper will be shared by the lead contact upon request.
- This paper does not report original code, but image analysis pipelines will be shared by the lead contact upon request.
- Any additional information required to reanalyze the data reported in this paper is available from the lead contact upon request.

EXPERIMENTAL MODEL AND SUBJECT DETAILS

Animals—Mice were housed and maintained in accordance with recommendations set in the Guide for the Care and Use of Laboratory Animals of the National Institutes of Health. All animal protocols were approved by the Icahn School of Medicine at Mount Sinai Institutional Animal Care and Use Committee (IACUC). Male and female mice were used for all experiments with the exception of the *Dmd*$^{mdx\text{-}4Cv}$ tissue clearing, in which all mice were hemizygous males. Mice were genotyped by PCR using toe DNA.

Mouse breeding—To generate the *Pax7*^{CreERT2};*ROSA26*$^{LSL\text{-}TdTomato}$ line, 8-12 week-old female homozygous *R26*$^{LSL\text{-}TdT}$ mice were purchased from Jackson Laboratory (Madisen et al., 2010) (007914) and crossed to 8-16 week-old male homozygous *Pax7*^{CreERT2} mice (Murphy et al., 2011) (Jackson Laboratory, 017763). *Rac1*$^{fl/+}$ and *Rac1*$^{fl/fl}$ mice were generated by crossing 8-12 week-old *Rac1*$^{fl/fl}$ homozygous females (Glogauer et al., 2003) (Jackson Laboratory, 005550) to 8-16 week-old male homozygous *Pax7*^{CreERT2};*R26*$^{LSL\text{-}TdT}$ mice. For the muscular dystrophy mouse model, 6-8 week-old female homozygous *Dmd*$^{mdx\text{-}4Cv}$ mice (Chapman, 1989; Shin et al., 2011) (Jackson Laboratory, 001801) were crossed to 8-16 week-old male homozygous *Pax7*^{CreERT2};*R26*$^{LSL\text{-}TdT}$ mice. Only hemizygous male offspring were used for experiments. To generate the N-cadherin conditional knockout mouse line, *Cdh2*$^{fl/fl}$;*Cdh15*$^{-/-}$;*Pax7*^{CreERT2} mice (Goel et al., 2017) (previously generated in our lab) were crossed to *Pax7*^{CreERT2};*R26*$^{LSL\text{-}TdT}$ mice (generation described above) and offspring were bred until homozygosity was reached for *Cdh2* alongside heterozygous alleles for *Pax7*^{CreERT2} and *R26*$^{LSL\text{-}TdT}$. *Tg:Pax7*^{nGFP} transgenic mice (Sambasivan et al., 2009) were obtained from the laboratory of Dr. Michael Rudnicki (The Ottawa Hospital Research Institute).

Muscle stem cell isolation for hydrogel culture—Muscle stem cells (SCs) were isolated from the hindlimb muscles of Pax7nGFP mice (Sambasivan et al., 2009) using an adaptation of published methods (Davoudi et al., 2018; Sacco et al., 2008). Briefly, the

muscles were dissected and digested with Collagenase, Dispase, and DNAse. Dissociated tissues were then passed through appropriate cell strainers and incubated in red blood cells lysis buffer. MuSCs were isolated with magnetic-activated cell sorting; non-SCs were depleted using the Satellite Cell Isolation Kit (Miltenyi Biotec 130-104-268) followed by enrichment of MuSCs using Anti-lntegrin α-7 MicroBeads (Miltenyi Biotec 130-104-261).

Primary MuSC culture—Isolated MuSCs were seeded on hydrogels immediately after sorting and cultured for 20-24hrs in DMEM + 2% bovine serum albumin ± 10μM ROCK inhibitor Y-27632 (StemCell Technologies, Inc. 72304).

METHOD DETAILS

Animal procedures—Adult mice (2-6 months) were injected intraperitoneally for 5 consecutive days with 200μL of a 7.5mg/mL tamoxifen solution (Sigma T5648) dissolved in corn oil. Control (*Pax7*^{CreERT};*R26*$^{LSL\text{-}TdT}$) and *Dmd*$^{mdx\text{-}4Cv}$ mice were harvested one week after tamoxifen delivery; *Rac1*$^{fl/+}$, *Rac1*$^{fl/fl}$, and *Cdh2*$^{fl/fl}$ mouse lines were harvested four weeks after delivery. For both injury techniques, adult mice (8-12 weeks) were anesthetized and shaved on the left hindlimb. For barium chloride injury, 1.2% barium chloride (Sigma-Aldrich 342920) was dissolved in saline and 50μL of the diluted barium chloride solution was injected into the tibialis anterior muscle as previously described (Tierney and Sacco, 2016). G_{alert} muscles were collected from contralateral limbs two days after $BaCl_2$ injury for analysis. For focal needle injury, a 32-gauge needle (Hamilton 7803-04) was used to puncture the distal end of the extensor digitorum longus (EDL) muscle five consecutive times.

Tissue clearing—Mice were anesthetized by isoflurane inhalation delivered via a precision vaporizer (VetEquip 911103), followed by cardiac perfusion with a peristaltic pump (Gilson F155006) set at 9 ml/minute, with room temperature (RT) PBS (plus 10 μg/ml heparin) for 1 minute to elute the blood, then RT 4% PFA for 7 minutes, then RT PBS for 3 minutes, followed by EDL muscle dissection. The extracted muscles were post-fixed in 4% PFA at 4°C overnight, then washed 3 times in PBS at RT for 1 hour. The fixed samples were delipidated following a modified Adipo-Clear protocol (Chi et al., 2018): The muscles were washed in a methanol/B1N buffer gradient (0%, 20%, 40%, 60%, 80% methanol; B1N buffer is H2O/0.1% Triton X-100/0.3 M glycine, pH7) for 15 minutes each step, twice with 100% methanol for 15 minutes, dichloridemethane for 30 minutes, and 3 times with 100% methanol for 15 minutes. Samples were rehydrated by washing in a reverse methanol/B1N gradient (80%, 60%, 40%, 20%) for 15 minutes each step, B1N for 1 hour, overnight with 5% DMSO/0.3M Glycine/PTxwH, and 3 times with PTxwH for 15 minutes (PTxwH is PBS/0.1% Triton X-100/0.05% Tween 20/2 mg/ml heparin). Muscles (3 EDL muscles per group) were immunostained with 2 μg goat anti-mCherry antibody (SICGEN AB0081-500) in 600 μl PTxwH at 37°C for 2 days, washed 3 times in PTxwH at 37°C for 2 hours, then stained with 12 μg Alexa Fluor 568-conjugated Donkey anti-Goat antibody (ThermoFisher Scientific A11057), with or without 5.2μg Mouse Alexa Fluor 647 preconjugated Mouse anti-Ncad antibody (Santa Cruz sc-8424 AF647) in 600 μl PTxwH at RT for 2 days. Samples were then washed 3 times in PTxwH at RT for 2 hours and further fixed in 1% PFA at 4°C overnight, washed in PTxwH at RT for 2 hours, then blocked in

B1N at RT overnight, and washed in PTxwH at RT for 2 hours. Samples were then bleached in 0.3% H_2O_2 at 4°C overnight, washed 3 times in 20mM PB at RT for 2 hours and twice with 25% 2,2'-thiodiethanol/10mM PBS at RT for 1 hour, and finally equilibrated with 75% Histodenz buffer (Cosmo Bio USA AXS-1002424) with refractive index adjusted to 1.53 using 2,2'-thiodiethanol to clear and mount on Concavity Microscope Slides (ThermoFisher Scientific 1527006) for imaging.

Single myofiber isolation and culture—Single myofibers were isolated from EDL muscles as previously described (Goel and Krauss, 2019), with the following modifications to preserve MuSC projections. When removing the EDL, it was essential that the tendon at the knee be cut prior to the tendon at the ankle (see Methods Video 1). Tugging on the muscle during excision must be avoided, as even minor stretch causes projection retraction and cell activation. Note that if there is resistance when sliding the EDL out, the tendons weren't properly severed. Isolated EDLs were incubated in plating media containing type I collagenase (2.6 mg/mL; Gibco 17100-017) in a 37°C shaking water bath for 53-55 minutes, followed by gentle trituration with a wide-mouth glass pipet in a 10 cm plate. After trituration, plates were placed in a 37°C incubator for 10 minutes to allow myofibers to straighten out. When myofibers were cultured in the presence of growth factors, 0.5% chick embryo extract (United States Biological Corporation, NC1202490) was added and the plate returned to the incubator. For fixation, myofibers were quickly transferred from the trituration plate to a new plate filled with PBS. After a brief wash (1 min), myofibers were fixed for 10 minutes in paraformaldehyde (final concentration of 4% in PBS). myofibers were washed in fresh PBS post-fixation and a dissection microscope was used to select straight, intact myofibers for use in immunofluorescence experiments.

***Ex vivo* treatment of single myofibers—**For all *ex vivo* treatment experiments, drugs were added to the media in both collagenase-containing digestion tubes and plates, allowing exposure immediately after muscle excision. myofibers were treated with Rho/MRTFA/SRF inhibitor CCG-203971 (10μM; Sigma-Aldrich SML1422), MEK1/2 inhibitor PD 0325901 (1μM; Sigma-Aldrich PZ0162), Rac inhibitor NSC23766 trihydrochloride (50μM; Sigma-Aldrich SML0952), or myosin II inhibitor Blebbistatin (25μM; Sigma-Aldrich B0560) and either collected immediately after trituration or cultured for set time points. Experiments using the ROCK inhibitor Y-27632 (StemCell Technologies, Inc. 72304) used a concentration of 50μM; key experiments were also performed using 10μM and produced statistically similar results. Myofibers were then fixed and stained with various antibodies.

$BaCl_2$ injury on single myofibers—Single myofibers were collected (see above) and cultured in the presence of either saline (control) or 1.2% $BaCl_2$ (Sigma-Aldrich 342920) in saline. myofibers were collected after 5 or 60 minutes, then washed with PBS and fixed in 4% PFA for 10 minutes.

Click-iT EdU incorporation in single myofiber cultures—Using the Click-iT EdU kit (ThermoFisher C10337), single myofibers were cultured in media containing 10μM EdU (and inhibitors, where applicable) for 30 hours. myofibers were isolated and fixed in PFA

as described above, washed three times with 3% BSA in PBS, permeabilized for 10 minutes in 0.2% Triton-X-100/PBS, then washed twice more with 3% BSA. The Click-iT reaction cocktail was prepared according to manufacturer directions, and myofibers were incubated in the cocktail for 30 minutes at room temperature in the dark. myofibers were washed once more with 3% BSA, three times with PBS, then mounted with DAPI-containing Fluoroshield (Abcam ab104139) for imaging.

Isolation and immunofluorescence of perfusion-fixed EDLs—Following perfusion fixation and EDL excision (see Tissue Clearing), whole muscles were washed in PBS and carefully separated at the tendons into 2-4 bundles of myofibers. Bundles were then washed 3 times in PBS for 5 minutes and 3 times in 0.2% Triton-X-100/PBS (PBST) for 15 minutes. Muscles were blocked with 10% goat serum for 1 hour at room temperature, followed by incubation with primary antibodies for 48 hours at 4°C on a shaker. Muscles were subsequently washed 3 times with PBS for 10 minutes, 3 times with PBST for 15 minutes, and blocked once more with 10% goat serum for 1 hour at room temperature. Secondary antibodies and Hoescht were added and samples were incubated for 48 hours at 4°C on a shaker. Following this incubation, samples were washed 3 times with PBS for 5 minutes and 6 times with PBS for 30 minutes before being mounted on microscopy slides.

Immunofluorescence (primary myofibers)—Briefly, fixed myofibers were permeabilized in 0.2% Triton-X-100/PBS (PBST) for 10 minutes, followed by the addition of 10% goat serum and blocking for 1 hour on a shaker. Primary antibodies were added and myofibers were incubated overnight at 4°C on a shaker. The following day, myofibers were washed once with PBS and 3 times with PBST, followed by addition of 10% goat serum for another hour of blocking. Secondary antibodies were added and myofibers were incubated for an hour in the dark. myofibers were then washed once with PBS and 3 times with PBST, then mounted with DAPI-containing Fluoroshield (Abcam ab104139).

Preparation of frozen muscle sections and immunohistochemistry—Following euthanization, tibialis anterior (TA) muscles were isolated and immediately mounted in 10% Tragacanth gum (Alfa Aesar A18502) and flash frozen in liquid nitrogen-cooled 2-methylbutane/isopentane (Fisher Scientific 03551-4). 10μm tissue sections were obtained with a Leica CM3050 S cryostat. Sections were fixed in 4% PFA for 20 minutes on ice, washed in PBS, then permeabilized in methanol for 6 minutes at −20°C. Antigen retrieval was performed with 0.01M citric acid pH 6.0. Following blocking, sections were incubated with primary antibodies overnight at 4°C. Secondary antibodies were added the following day following washing and blocking. Sections were mounted DAPI-containing Fluoroshield (Abcam ab104139).

Immunocytochemistry (primary MuSC culture)—SCs were fixed with 4% PFA for 15 minutes, then permeabilized and blocked with a solution containing 10% goat serum, 1 % bovine serum albumin (BioShop Canada ALB005.100) and 0.1% Triton X–100 diluted in PBS for 30 minutes at RT. Subsequently, samples were incubated in primary antibodies (mouse anti-α-Tubulin (GeneTex GT114) and chicken anti-GFP (Novus Biologicals NB100-1614)) diluted in 5% goat serum in PBS) for 20-24hrs at 4°C, and then

in secondary antibodies (goat anti-mouse IgG, Alexa Fluor 546 (Invitrogen A-11003) and goat anti-Chicken IgY, Alexa Fluor 488 (Invitrogen A-11039)) for 1 hour at RT the next day, followed by counterstaining with Hoechst 33342 for 10 minutes. Samples were washed in PBS 3 times for 5 minutes each time in between all steps except after blocking. We note that the GFP signal diffuses slightly to the cytoplasm and is amplified by the anti-GFP antibody (see Figure 4L).

***In situ* binding assays for GTPase activity—**Fixed myofibers were permeabilized with 0.2% Triton-X-100/PBS (PBST) for 10 minutes, followed by the addition of 10% goat serum and blocking for 1 hour on a shaker. myofibers were then incubated for 1 hour with GST-tagged Rhotekin-Rho binding domain (RBD) (Cytoskeleton RT01) or GST-tagged Pak1-p21 binding domain (PBD) (Cytoskeleton PAK01) proteins, which serve as readouts for active Rho or active Rac/Cdc42, respectively. myofibers were washed 3 times with PBS, then incubated in the presence of Alexa Fluor 488-conjugated anti-GST antibody (Invitrogen A-11131) for 1 hour. After incubation, myofibers were washed and mounted with DAPI-containing Fluoroshield (Abcam ab104139).

Hydrogel fabrication—Polyacrylamide hydrogels with Young's moduli of 40 kPa were fabricated as previously described (Tse and Engler, 2010). Briefly, acrylamide and bis-acrylamide were combined and added to chloro-silanized glass slides. Amino-silanized coverslips were added on top, sandwiching the polymerizing solution in between the glass slide and the coverslip. After polymerization, gels were tethered with laminin (Roche 11243217001).

QUANTIFICATION AND STATISTICAL ANALYSES

Imaging and post-image analysis—For the hydrogel cultures, representative images were obtained using a Zeiss Axio Observer 7 confocal microscope equipped with a LSM 800 scan head and Plan-APO 40x/1.40 Oil DIC objective. Immunohistochemistry images were obtained using a Zeiss Axio Imager Z2 upright microscope equipped with a 20x/0.75 air objective. All other images were collected using 40x/1.25 or 63x/1.40 Oil fluorescent objectives on a Leica DMI SP8 inverted confocal microscope, equipped with Leica Application Suite. Filter settings, gain and exposure values were kept consistent between experiments. Z-stacks were collected for all tissue clearing experiments and where necessary to capture full projection lengths on single myofibers (step size of 1-2μm). Line averaging was used on representative images to improve signal-to-noise ratio; line average=3, frame average=2. Images were exported to ImageJ for post-imaging analysis, including adjustment of brightness/contrast and generation of maximum intensity projections.

Image quantifications—Images for hydrogel quantifications were obtained using an Olympus IX83 inverted microscope. Images for immunohistochemistry quantifications were obtained using a Zeiss Axio Imager Z2 upright microscope. 10 random images per genotype were taken at 20x magnification. All other images were obtained using a Leica DMI SP8 microscope. .tif files were exported for quantification using in ImageJ or CellProfiler (Carpenter et al., 2006).

- **Projection lengths:** Projection lengths were quantified using FIJI's Measure function and converted from px to μm using image scale bars as a reference. 'Projections' were defined as the distance between the end of the nucleus to the outermost tip of each cell; in the case of multiple projections, lengths were added together. For tissue clearing experiments, random z-stacks (100μm depth) were taken of each EDL, and ~50 independent cells were quantified per muscle. For quantification of projection lengths and percentages of cells with projections on myofibers, 50-75 cells were scored and quantified per mouse.
- **Projection angles:** Using Z-stacks of cleared muscle, FIJI's Measure function was used to identify the angle of MuSC projections and the longitudinal angle of the myofiber associated with each cell. The difference between the two values was calculated as a measurement of projection angle.
- **Ddx6$^+$ granule quantifications:** Single muscle myofibers were stained for Ddx6, and multi-channel images of each cell were taken. A custom CellProfiler pipeline was used to perform a threshold function on the Pax7-TdT channel, followed by identification of the MuSC as a primary object. Ddx6 puncta were brightened using the EnhanceOrSuppressFeatures module for enhancing speckles, then the Pax7-TdT channel was used to mask the enhanced Ddx6 image. Ddx6 puncta were identified as primary objects (min-max range of 2-100 px), then related back to their parent Pax7-TdT objects.
- **Circularity index measurement of MuSC nuclei:** To quantify circularity of nuclei, images of DAPI-stained MuSC nuclei were run through a custom CellProfiler pipeline. A threshold function was performed on DAPI channel images, the binary image was then identified as a primary object, and the Eccentricity of the object was quantified through the MeasureObjectSizeShape module. Eccentricity is defined as the ratio of the distance between the foci of an ellipse and its major axis length. To calculate circularity, each value was subtracted from 1, yielding a range from 0-1 (in which 0 is a straight line, and 1 is a perfect circle).
- **GTPase intensity measurement:** In situ binding assays for Pak1GST and RhoGST were performed on single muscle myofibers, and multi-channel images were taken of each cell. A custom CellProfiler pipeline was used to perform a threshold function on the Pax7-TdT channel, identifying the MuSC as a primary object. This image was then used as a mask on the Pak1GST/RhotekinGST channel image, and the integrated intensity of the masked image was quantified. Any background myofiber signal was quantified, averaged, and subtracted from the intensity values.
- **MYOD intensity measurement:** Following MYOD immunofluorescence on single myofibers, multi-channel images were taken of each MuSC. A CellProfiler pipeline performed a thresholding function on the Pax7-TdT channel, identifying the MuSC as a primary object. This object was then used to isolate MuSC nuclei within the DAPI channel, setting the MuSC nucleus as

a secondary object. The MuSC nucleus was next used as a mask on the MYOD channel image, and the integrated intensity of the MYOD signal was quantified.

Statistical analysis—Tissue clearing and $Rac^{fl/+}$ experiments were performed with n=3 mice; all other experiments were performed with at least n=4 mice, of which 4 random, representative samples were used for quantification. All immunofluorescence experiments included quantification of ~50 independent cells per time point/treatment condition, averaged to yield mean values per mouse that were then used for statistical analysis. The experiments using small molecule inhibitors required that entire EDL muscles be excised directly into inhibitor-containing medium for myofiber preparation. Consequently, it was not possible to use myofibers from this same muscle as controls. For inhibitor-treated preparations, control myofibers were assessed in parallel with drug-treated myofibers and all datasets were quantified together (one-way ANOVA with multiple comparisons test rather than repeated individual *t*-tests between control and single inhibitor datasets) before being split into individual figures for publication. The control values are therefore repeated across multiple figures, as described in figure legends. Specifically, the GTPase inhibitors in Fig. 3–4 and S3–S4 share a control data set, and the MEK/MRTFA inhibitors in Fig. 5 and S5 share a different control data set. Representative immunofluorescence images without quantifications were performed at least three times with reproducible results. A two-tailed unpaired *t*-test with Welch's correction was used to compare data between two independent groups. Data with more than two independent groups were analyzed by one-way ANOVA with Bonferroni's multiple comparisons test. Data with two or more factors were analyzed using two-way ANOVA with Bonferroni's multiple comparisons test orTukey's multiple comparisons test (stated in figure legends). Data assessing changes in one condition over different time points were analyzed by one-way ANOVA with Šídák's multiple comparisons test. *P* values were obtained using GraphPad PRISM and used to determine the level of varying significance between experimental groups; groups were considered different when $P<0.05$.

Supplementary Material

Refer to Web version on PubMed Central for supplementary material.

ACKNOWLEDGEMENTS

We thank Anna Kolstad for assistance with perfusion experiments and Philippe Soriano, Paul Wassarman, and Nicole Dubois for critical reading of the manuscript. This work was funded by a National Institute of Arthritis and Musculoskeletal and Skin Diseases grant to R.S.K. (AR070231), a Natural Sciences and Engineering Research Council grant to P.M.G. (RGPIN-2019-07144), a fellowship of the Training Program in Stem Cell Research from the New York State Department of Health to A.P.K. (NYSTEM-C32561GG), an National Institute of Child Health and Development Training Grant fellowship to M.H. (T32 HD075735), a Connaught International Scholarship and Cecil Yip Doctoral Award to J.N., and the Tisch Cancer Institute at the Icahn School of Medicine at Mount Sinai (P30 CA196521 – Cancer Center Support Grant). Microscopy was performed at the Microscopy CoRE at the Icahn School of Medicine at Mount Sinai. Model images and schematics were created with BioRender.com.

REFERENCES

Almada AE, Horwitz N, Price FD, Gonzalez AE, Ko M, Bolukbasi OV, Messemer KA, Chen S, Sinha M, Rubin LL, and Wagers AJ (2021). FOS licenses early events in stem cell activation driving skeletal muscle regeneration. Cell Rep 34, 108656. [PubMed: 33503437]

Aragona M, Sifrim A, Malfait M, Song Y, Van Herck J, Dekoninck S, Gargouri S, Lapouge G, Swedlund B, Dubois C, et al. (2020). Mechanisms of stretch-mediated skin expansion at single-cell resolution. Nature 584, 268–273. [PubMed: 32728211]

Baghdadi MB, Firmino J, Soni K, Evano B, Di Girolamo D, Mourikis P, Castel D, and Tajbakhsh S (2018). Notch-Induced miR-708 Antagonizes Satellite Cell Migration and Maintains Quiescence. Cell Stem Cell 23, 859–868. [PubMed: 30416072]

Bar-Sagi D, and Hall A (2000). Ras and Rho GTPases: A Family Reunion. Cell 103, 227–238. [PubMed: 11057896]

Bentzinger CF, von Maltzahn J, Dumont NA, Stark DA, Wang YX, Nhan K, Frenette J, Cornelison DD, and Rudnicki MA (2014). Wnt7a stimulates myogenic stem cell motility and engraftment resulting in improved muscle strength. J Cell Biol 205, 97–111. [PubMed: 24711502]

Bernier LP, Bohlen CJ, York EM, Choi HB, Kamyabi A, Dissing-Olesen L, Hefendehl JK, Collins HY, Stevens B, Barres BA, and MacVicar BA (2019). Nanoscale Surveillance of the Brain by Microglia via cAMP-Regulated Filopodia. Cell Rep 27, 2895–2908. [PubMed: 31167136]

Bhadriraju K, Yang M, Alom Ruiz S, Pirone D, Tan J, and Chen CS (2007). Activation of ROCK by RhoA is regulated by cell adhesion, shape, and cytoskeletal tension. Exp Cell Res 313, 3616–3623. [PubMed: 17673200]

Brack AS, and Rando TA (2012). Tissue-specific stem cells: lessons from the skeletal muscle satellite cell. Cell Stem Cell 10, 504–514. [PubMed: 22560074]

Burridge K, and Wennerberg K (2004). Rho and Rac Take Center Stage. Cell 116, 167–179. [PubMed: 14744429]

Buszczak M, Inaba M, and Yamashita YM (2016). Signaling by Cellular Protrusions: Keeping the Conversation Private. Trends Cell Biol 26, 526–534. [PubMed: 27032616]

Byrne KM, Monsefi N, Dawson JC, Degasperi A, Bukowski-Wills JC, Volinsky N, Dobrzynski M, Birtwistle MR, Tsyganov MA, Kiyatkin A, et al. (2016). Bistability in the Rac1, PAK, and RhoA Signaling Network Drives Actin Cytoskeleton Dynamics and Cell Motility Switches. Cell Syst 2, 38–48. [PubMed: 27136688]

Carpenter AE, Jones TR, Lamprecht MR, Clarke C, Kang I, Friman O, Guertin DA, Chang J, Lindquist RA, Moffat J, et al. (2006). CellProfiler: image analysis software for identifying and quantifying cell phenotypes. Genome Biology 7. 10.1186/gb-2006-7-10-r100.

Cen B, Selvaraj A, and Prywes R (2004). Myocardin/MKL family of SRF coactivators: key regulators of immediate early and muscle specific gene expression. J Cell Biochem 93, 74–82. [PubMed: 15352164]

Chakkalakal JV, Jones KM, Basson MA, and Brack AS (2012). The aged niche disrupts muscle stem cell quiescence. Nature 490, 355–360. [PubMed: 23023126]

Chapman VM, Miller DR, Armstrong D, and Caskey CT (1989). Recovery of induced mutations for X chromosome-linked muscular dystrophy in mice. Proc Natl Acad Sci U S A 86, 1292–1296. [PubMed: 2919177]

Chi J, Crane A, Wu Z, and Cohen P (2018). Adipo-Clear: A Tissue Clearing Method for Three-Dimensional Imaging of Adipose Tissue. J Vis Exp. 10.3791/58271.

Crist CG, Montarras D, and Buckingham M (2012). Muscle satellite cells are primed for myogenesis but maintain quiescence with sequestration of Myf5 mRNA targeted by microRNA-31 in mRNP granules. Cell Stem Cell 11, 118–126. [PubMed: 22770245]

Davoudi S, Chin CY, Cooke MJ, Tam RY, Shoichet MS, and Gilbert PM (2018). Muscle stem cell intramuscular delivery within hyaluronan methylcellulose improves engraftment efficiency and dispersion. Biomaterials 173, 34–46. [PubMed: 29738956]

de Morree A, van Velthoven CTJ, Gan Q, Salvi JS, Klein JDD, Akimenko I, Quarta M, Biressi S, and Rando TA (2017). Staufen1 inhibits MyoD translation to actively maintain muscle stem cell quiescence. Proc Natl Acad Sci U S A 114, E8996–E9005. [PubMed: 29073096]

De Wever O, Westbroek W, Verloes A, Bloemen N, Bracke M, Gespach C, Bruyneel E, and Mareel M (2004). Critical role of N-cadherin in myofibroblast invasion and migration in vitro stimulated by colon-cancer-cell-derived TGF-beta or wounding. J Cell Sci 117, 4691–4703. [PubMed: 15331629]

Der Vartanian A, Quetin M, Michineau S, Aurade F, Hayashi S, Dubois C, Rocancourt D, Drayton-Libotte B, Szegedi A, Buckingham M, et al. (2019). PAX3 Confers Functional Heterogeneity in Skeletal Muscle Stem Cell Responses to Environmental Stress. Cell Stem Cell 24, 958–973 e959. [PubMed: 31006622]

Dogterom M, and Koenderink GH (2019). Actin-microtubule crosstalk in cell biology. Nat Rev Mol Cell Biol 20, 38–54. [PubMed: 30323238]

Dupraz S, Hilton BJ, Husch A, Santos TE, Coles CH, Stern S, Brakebusch C, and Bradke F (2019). RhoA Controls Axon Extension Independent of Specification in the Developing Brain. Curr Biol 29, 3874–3886 e3879. [PubMed: 31679934]

El-Sibai M, Pertz O, Pang H, Yip SC, Lorenz M, Symons M, Condeelis JS, Hahn KM, and Backer JM (2008). RhoA/ROCK-mediated switching between Cdc42- and Rac1-dependent protrusion in MTLn3 carcinoma cells. Exp Cell Res 314, 1540–1552. [PubMed: 18316075]

Eliazer S, Muncie JM, Christensen J, Sun X, D'Urso RS, Weaver VM, and Brack AS (2019). Wnt4 from the Niche Controls the Mechano-Properties and Quiescent State of Muscle Stem Cells. Cell Stem Cell 25, 654–665 e654. [PubMed: 31495781]

Endow SA, Miller SE, and Ly PT (2019). Mitochondria-enriched protrusions are associated with brain and intestinal stem cells in Drosophila. Commun Biol 2, 427. 10.1038/s42003-019-0671-4. [PubMed: 31799429]

Fukata M, and Kaibuchi K (2001). Rho-family GTPases in cadherin-mediated cell-cell adhesion. Nat Rev Mol Cell Biol 2, 887–897. [PubMed: 11733768]

Gengatharan A, Malvaut S, Marymonchyk A, Ghareghani M, Snapyan M, Fischer-Sternjak J, Ninkovic J, Gotz M, and Saghatelyan A (2021). Adult neural stem cell activation in mice is regulated by the day/night cycle and intracellular calcium dynamics. Cell 184, 709–722. [PubMed: 33482084]

Gilbert PM, Havenstrite KL, Magnusson KE, Sacco A, Leonardi NA, Kraft P, Nguyen NK, Thrun S, Lutolf MP, and Blau HM (2010). Substrate elasticity regulates skeletal muscle stem cell self-renewal in culture. Science 329, 1078–1081. [PubMed: 20647425]

Glogauer M, Marchal CC, Zhu F, Worku A, Clausen BE, Foerster I, Marks P, Downey GP, Dinauer M, and Kwiatkowski DJ (2003). Rac1 deletion in mouse neutrophils has selective effects on neutrophil functions. J Immunol 170, 5652–5657. [PubMed: 12759446]

Goel AJ, and Krauss RS (2019). Ex Vivo Visualization and Analysis of the Muscle Stem Cell Niche. Methods Mol Biol 2002, 39–50. [PubMed: 30178310]

Goel AJ, Rieder MK, Arnold HH, Radice GL, and Krauss RS (2017). Niche Cadherins Control the Quiescence-to-Activation Transition in Muscle Stem Cells. Cell Rep 21, 2236–2250. [PubMed: 29166613]

Gould RA, Yalcin HC, MacKay JL, Sauls K, Norris R, Kumar S, and Butcher JT (2016). Cyclic Mechanical Loading Is Essential for Rac1-Mediated Elongation and Remodeling of the Embryonic Mitral Valve. Curr Biol 26, 27–37. [PubMed: 26725196]

Guilluy C, Garcia-Mata R, and Burridge K (2011). Rho protein crosstalk: another social network? Trends Cell Biol 21, 718–726. [PubMed: 21924908]

Haroon M, Klein-Nulend J, Bakker AD, Jin J, Seddiqi H, Offringa C, de Wit GMJ, Le Grand F, Giordani L, Liu KJ, et al. (2021). Myofiber stretch induces tensile and shear deformation of muscle stem cells in their native niche. Biophys J 120, 2665–2678. [PubMed: 34087215]

Hausburg MA, Doles JD, Clement SL, Cadwallader AB, Hall MN, Blackshear PJ, Lykke-Andersen J, and Olwin BB (2015). Post-transcriptional regulation of satellite cell quiescence by TTP-mediated mRNA decay. Elife 4, e03390. [PubMed: 25815583]

Hirano K, Tsuchiya M, Takabayashi S, Nagao K, Kitajima Y, Ono Y, Nonomura K, Mori Y, Umeda M, and Hara Y (2021). The mechanosensitive Ca2+-permeable ion channel PIEZO1 promotes satellite cell function in skeletal muscle regeneration. bioRxiv. 10.1101/2021.03.18.435982.

Hollnagel A, Grund C, Franke WW, and Arnold HH (2002). The cell adhesion molecule M-cadherin is not essential for muscle development and regeneration. Mol Cell Biol 22, 4760–4770. [PubMed: 12052883]

Hutchings KM, Lisabeth EM, Rajeswaran W, Wilson MW, Sorenson RJ, Campbell PL, Ruth JH, Amin A, Tsou PS, Leipprandt JR, et al. (2017). Pharmacokinetic optimitzation of CCG-203971: Novel

inhibitors of the Rho/MRTF/SRF transcriptional pathway as potential antifibrotic therapeutics for systemic scleroderma. Bioorg Med Chem Lett 27, 1744–1749. [PubMed: 28285914]

Inaba M, Buszczak M, and Yamashita YM (2015). Nanotubes mediate niche-stem-cell signalling in the Drosophila testis. Nature 523, 329–332. [PubMed: 26131929]

Jossin Y, and Cooper JA (2011). Reelin, Rap1 and N-cadherin orient the migration of multipolar neurons in the developing neocortex. Nat Neurosci 14, 697–703. [PubMed: 21516100]

Kalpachidou T, Spiecker L, Kress M, and Quarta S (2019). Rho GTPases in the Physiology and Pathophysiology of Peripheral Sensory Neurons. Cells 8. 10.3390/cells8060591.

Kim SH, Li Z, and Sacks DB (2000). E-cadherin-mediated cell-cell attachment activates Cdc42. J Biol Chem 275, 36999–37005. [PubMed: 10950951]

Kimura K, Ito M, Amano M, Chihara K, Fukata Y, Nakafuku M, Yamamori B, Feng J, Nakano T, Okawa K, et al. (1996). Regulation of Myosin Phosphatase by Rho and Rho-Associated Kinase (Rho-Kinase). Science 273, 245–248. [PubMed: 8662509]

Korobova F, and Svitkina T (2008). Arp2/3 complex is important for filopodia formation, growth cone motility, and neuritogenesis in neuronal cells. Mol Biol Cell 19, 1561–1574. [PubMed: 18256280]

Kraemer A, Goodwin M, Verma S, Yap AS, and Ali RG (2007). Rac is a dominant regulator of cadherin-directed actin assembly that is activated by adhesive ligation independently of Tiam1. Am J Physiol Cell Physiol 292, C1061–1069. [PubMed: 17020937]

Linden LM, Gordon KL, Pani AM, Payne SG, Garde A, Burkholder D, Chi Q, Goldstein B, and Sherwood DR (2017). Identification of regulators of germ stem cell enwrapment by its niche in C. elegans. Dev Biol 429, 271–284. [PubMed: 28648843]

Lu M, and Krauss RS (2010). N-cadherin ligation, but not Sonic hedgehog binding, initiates Cdo-dependent p38 / MAPK signaling in skeletal myoblasts. Proceedings of the National Academy of Sciences 107, 4212–4217.

Liu L, Cheung TH, Charville GW, Hurgo BM, Leavitt T, Shih J, Brunet A, and Rando TA (2013). Chromatin modifications as determinants of muscle stem cell quiescence and chronological aging. Cell Rep 4, 189–204. 10.1016/j.celrep.2013.05.043. [PubMed: 23810552]

Lutolf MP, Gilbert PM, and Blau HM (2009). Designing materials to direct stem-cell fate. Nature 462, 433–441. [PubMed: 19940913]

Ma N, Chen D, Lee J-H, Kuri P, Hernandez EB, Kocan J, Mahmood H, Tichy ED, Rompolas P, and Mourkioti F (2022). Piezo1 regulates the regenerative capacity of skeletal muscles via orchestration of stem cell morphological states. Sci Adv 8, eabn0485. [PubMed: 35302846]

Machado L, Esteves de Lima J, Fabre O, Proux C, Legendre R, Szegedi A, Varet H, Ingerslev LR, Barres R, Relaix F, and Mourikis P (2017). In Situ Fixation Redefines Quiescence and Early Activation of Skeletal Muscle Stem Cells. Cell Rep 21, 1982–1993. [PubMed: 29141227]

Machado L, Geara P, Camps J, Dos Santos M, Teixeira-Clerc F, Van Herck J, Varet H, Legendre R, Pawlotsky JM, Sampaolesi M, et al. (2021). Tissue damage induces a conserved stress response that initiates quiescent muscle stem cell activation. Cell Stem Cell 28, 1125–1135. [PubMed: 33609440]

Madisen L, Zwingman TA, Sunkin SM, Oh SW, Zariwala HA, Gu H, Ng LL, Palmiter RD, Hawrylycz MJ, Jones AR, et al. (2010). A robust and high-throughput Cre reporting and characterization system for the whole mouse brain. Nat Neurosci 13, 133–140. [PubMed: 20023653]

Miralles F, Posern G, Zaromytidou A-I, Treisman R. (2003). Actin Dynamics Control SRF Activity by Regulation of its Coactivator MAL. Cell 113, 329–342. [PubMed: 12732141]

Morton AB, Norton CE, Jacobsen NL, Fernando CA, Cornelison DDW, and Segal SS. (2019). Barium chloride injures myofibers through calcium-induced proteolysis with fragmentation of motor nerves and microvessels. Skelet Muscle 9, 27. [PubMed: 31694693]

Muir AR, Kanji AHM, and Allbrook D (1965). The structure of the satellite cells in skeletal muscle. J. Anat 99, 435–444. [PubMed: 5857082]

Murphy MM, Lawson JA, Mathew SJ, Hutcheson DA, and Kardon G (2011). Satellite cells, connective tissue fibroblasts and their interactions are crucial for muscle regeneration. Development 138, 3625–3637. [PubMed: 21828091]

Niethammer P (2016). The early wound signals. Curr Opin Genet Dev 40, 17–22. [PubMed: 27266971]

Pardo-Pastor C, Rubio-Moscardo F, Vogel-Gonzalez M, Serra SA, Afthinos A, Mrkonjic S, Destaing O, Abenza JF, Fernandez-Fernandez JM, Trepat X, et al. (2018). Piezo2 channel regulates RhoA and actin cytoskeleton to promote cell mechanobiological responses. Proc Natl Acad Sci U S A 115, 1925–1930. [PubMed: 29432180]

Pasut A, Jones AE, and Rudnicki MA (2013). Isolation and culture of individual myofibers and their satellite cells from adult skeletal muscle. J Vis Exp, e50074. [PubMed: 23542587]

Prinz M, Jung S, and Priller J (2019). Microglia Biology: One Century of Evolving Concepts. Cell 179, 292–311. [PubMed: 31585077]

Priya R, Gomez GA, Budnar S, Verma S, Cox HL, Hamilton NA, and Yap AS (2015). Feedback regulation through myosin II confers robustness on RhoA signalling at E-cadherin junctions. Nat Cell Biol 17, 1282–1293. [PubMed: 26368311]

Provenzano PP, and Keely PJ (2011). Mechanical signaling through the cytoskeleton regulates cell proliferation by coordinated focal adhesion and Rho GTPase signaling. J Cell Sci 124, 1195–1205. [PubMed: 21444750]

Quarta M, Brett JO, DiMarco R, De Morree A, Boutet SC, Chacon R, Gibbons MC, Garcia VA, Su J, Shrager JB, et al. (2016). An artificial niche preserves the quiescence of muscle stem cells and enhances their therapeutic efficacy. Nat Biotechnol 34, 752–759. [PubMed: 27240197]

Randrianarison-Huetz V, Papaefthymiou A, Herledan G, Noviello C, Faradova U, Collard L , Pincini A, Schol E, Decaux JF, Maire P, et al. (2018). Srf controls satellite cell fusion through the maintenance of actin architecture. Journal of Cell Biology 217, 685–700. [PubMed: 29269426]

Reed F, Larsuel ST, Mayday MY, Scanlon V, and Krause DS (2021). MRTFA: A critical protein in normal and malignant hematopoiesis and beyond. J Biol Chem 296, 100543. [PubMed: 33722605]

Rodgers JT, King KY, Brett JO, Cromie MJ, Charville GW, Maguire KK, Brunson C, Mastey N, Liu L, Tsai CR, et al. (2014). mTORC1 controls the adaptive transition of quiescent stem cells from G0 to G(Alert). Nature 510, 393–396. [PubMed: 24870234]

Rozo M, Li L, and Fan C-M (2016). Targeting β1 -integrin signaling enhances regeneration in aged and dystrophic muscle in mice. Nat Med 22, 889–896. [PubMed: 27376575]

Sacco A, Doyonnas R, Kraft P, Vitorovic S, and Blau HM (2008). Self-renewal and expansion of single transplanted muscle stem cells. Nature 456, 502–506. [PubMed: 18806774]

Sacco A, Mourkioti F, Tran R, Choi J, Llewellyn M, Kraft P, Shkreli M, Delp S, Pomerantz JH, Artandi SE, and Blau HM (2010). Short telomeres and stem cell exhaustion model Duchenne muscular dystrophy in mdx/mTR mice. Cell 143, 1059–1071. [PubMed: 21145579]

Sakurada S, Takuwa N, Sugimoto N, Wang Y, Seto M, Sasaki Y, and Takuwa Y (2003). Ca2+-dependent activation of Rho and Rho kinase in membrane depolarization-induced and receptor stimulation-induced vascular smooth muscle contraction. Circ Res 93, 548–556. [PubMed: 12919947]

Sambasivan R, Gayraud-Morel B, Dumas G, Cimper C, Paisant S, Kelly RG, and Tajbakhsh S (2009). Distinct regulatory cascades govern extraocular and pharyngeal arch muscle progenitor cell fates. Dev Cell 16, 810–821. [PubMed: 19531352]

Schmalbruch H (1978). Satellite cells of rat muscles as studied by freeze-fracturing. Anat. Rac 191, 371–376.

Sheng M, and Greenberg ME (1990). The regulation and function of c-fos and other immediate early genes in the nervous system. Neuron 4, 477–485. [PubMed: 1969743]

Shin JH, Hakim CH, Zhang K, and Duan D (2011). Genotyping mdx, mdx3cv, and mdx4cv mice by primer competition polymerase chain reaction. Muscle Nerve 43, 283–286. [PubMed: 21254096]

Snyder JC, Rochelle LK, Marion S, Lyerly HK, Barak LS, and Caron MG (2015). Lgr4 and Lgr5 drive the formation of long actin-rich cytoneme-like membrane protrusions. J Cell Sci 128, 1230–1240. [PubMed: 25653388]

Takemura M, Mishima T, Wang Y, Kasahara J, Fukunaga K, Ohashi K, and Mizuno K (2009). Ca2+/calmodulin-dependent protein kinase IV-mediated LIM kinase activation is critical for calcium signal-induced neurite outgrowth. J Biol Chem 284, 28554–28562. [PubMed: 19696021]

Tierney MT, and Sacco A (2016). Inducing and Evaluating Skeletal Muscle Injury by Notexin and Barium Chloride. Methods Mol Biol 1460, 53–60. [PubMed: 27492165]

Tse JR, and Engler AJ (2010). Preparation of hydrogel substrates with tunable mechanical properties. Curr Protoc Cell Biol Chapter 10, Unit 10 16. 10.1002/0471143030.cb1016s47.

van den Brink SC, Sage F, Vértesy Á, Spanjaard B, Peterson-Maduro J, Baron CS, Robin C, and van Oudenaarden A (2017). Single-cell sequencing reveals dissociation-induced gene expression in tissue subpopulations. Nat Methods 14 (10), 935–936. [PubMed: 28960196]

van Velthoven CTJ, de Morree A, Egner IM, Brett JO, and Rando TA (2017). Transcriptional Profiling of Quiescent Muscle Stem Cells In Vivo. Cell Rep 21, 1994–2004. [PubMed: 29141228]

Verma M, Asakura Y, Murakonda BSR, Pengo T, Latroche C, Chazaud B, McLoon LK, and Asakura A (2018). Muscle Satellite Cell Cross-Talk with a Vascular Niche Maintains Quiescence via VEGF and Notch Signaling. Cell Stem Cell 23, 530–543. [PubMed: 30290177]

Wang X, Weisleder N, Collet C, Zhou J, Chu Y, Hirata Y, Zhao X, Pan Z, Brotto M, Cheng H, and Ma J (2005). Uncontrolled calcium sparks act as a dystrophic signal for mammalian skeletal muscle. Nat Cell Biol 7, 525–530. [PubMed: 15834406]

Webster MT, Manor U, Lippincott-Schwartz J, and Fan CM (2016). Intravital Imaging Reveals Ghost Fibers as Architectural Units Guiding Myogenic Progenitors during Regeneration. Cell Stem Cell 18, 243–252. [PubMed: 26686466]

Yin H, Price F, and Rudnicki MA (2013). Satellite cells and the muscle stem cell niche. Physiol Rev 93, 23–67. [PubMed: 23303905]

Yue L, Wan R, Luan S, Zeng W, and Cheung TH (2020). Dek Modulates Global Intron Retention during Muscle Stem Cells Quiescence Exit. Dev Cell 53, 661–676. [PubMed: 32502396]

Highlights:

- Quiescent muscle stem cell (MuSC) morphology can be preserved *ex vivo*
- MuSC activation is mediated by a Rac-to-Rho GTPase switch
- The Rho/ROCK/MLC pathway drives projection retraction
- Induction of the early gene *Fos* is initiated through Rho/MRTFA signaling

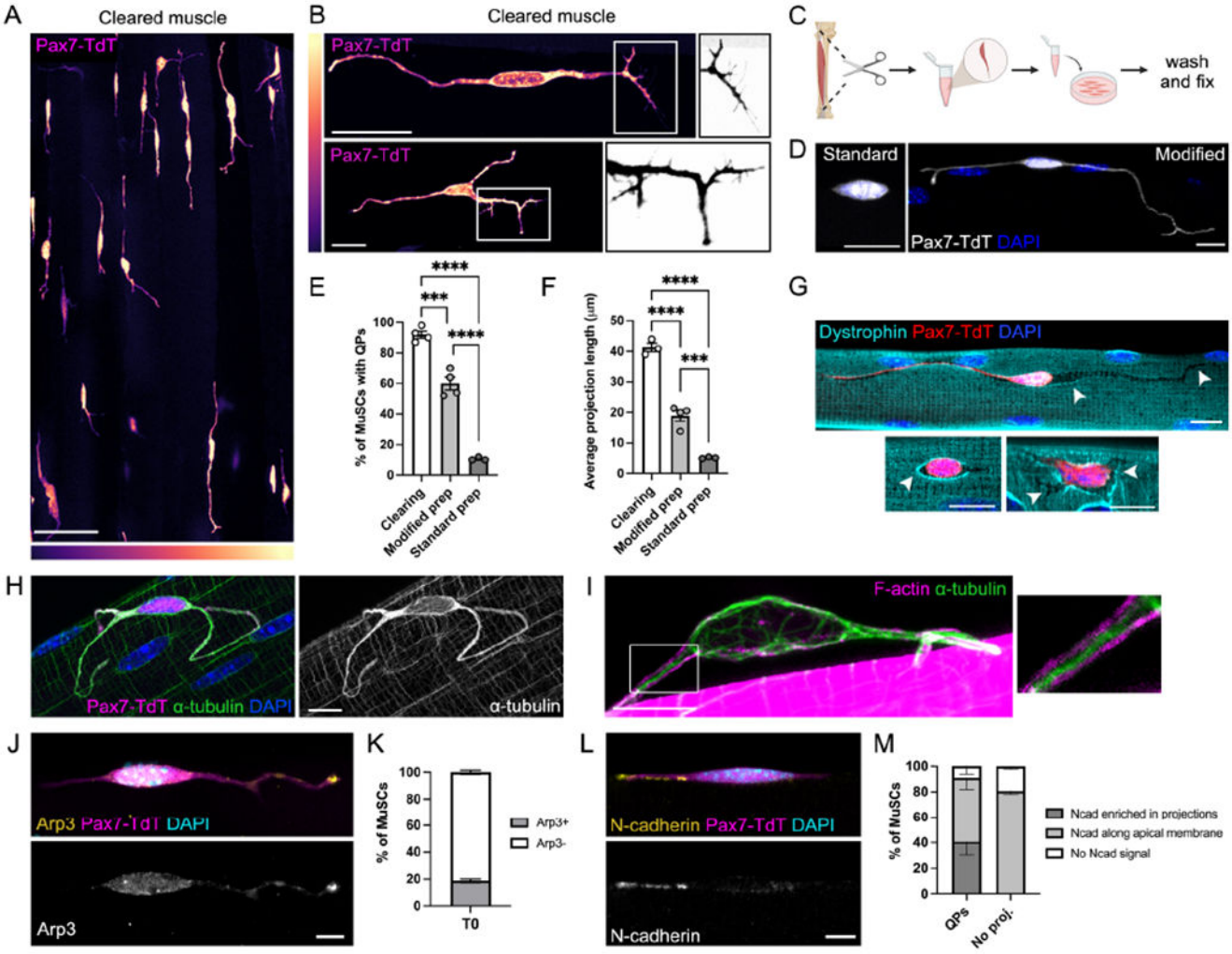

Figure 1. Quiescent MuSCs have long projections resembling motile structures.

(A-B) Cleared EDL muscle from *Pax7*^{CreERr2};*R26*$^{LSL\text{-}TdTom}$(Pax7-TdT) mice showing quiescent projections (QPs) in uninjured muscle (A) and individual MuSCs (B). Boxed regions in (B) are inverted and decolorized to show filopodia. LUTs indicate signal intensity. **(C)** Schematic showing single myofiber protocol. **(D)** MuSCs from the standard vs. modified myofiber protocol. **(E-F)** Quantifications of QP frequency (E) and lengths (F) from cleared muscle, modified, and standard myofiber preparations. **(G-I)** MuSCs showing grooves in the sarcolemma (G, arrowheads indicate sites of recent retraction), a dense α-tubulin network (H), and a cortical actin cytoskeleton in QPs (I). **(J-M)** Images and quantifications of Arp3 (J-K) or N-cadherin (L-M) localization in MuSCs. Data represent n=3-4 mice and show mean ± s.e.m.. Comparisons by one-way ANOVA with Bonferroni's multiple comparisons test (E-F); ***= p<0.001, ****= p<0.0001. Scale bars: (A) 50μm; (B) 25μm; (D,G) 10μm; (H-I,J,L) 5μm. See also Figure S1.

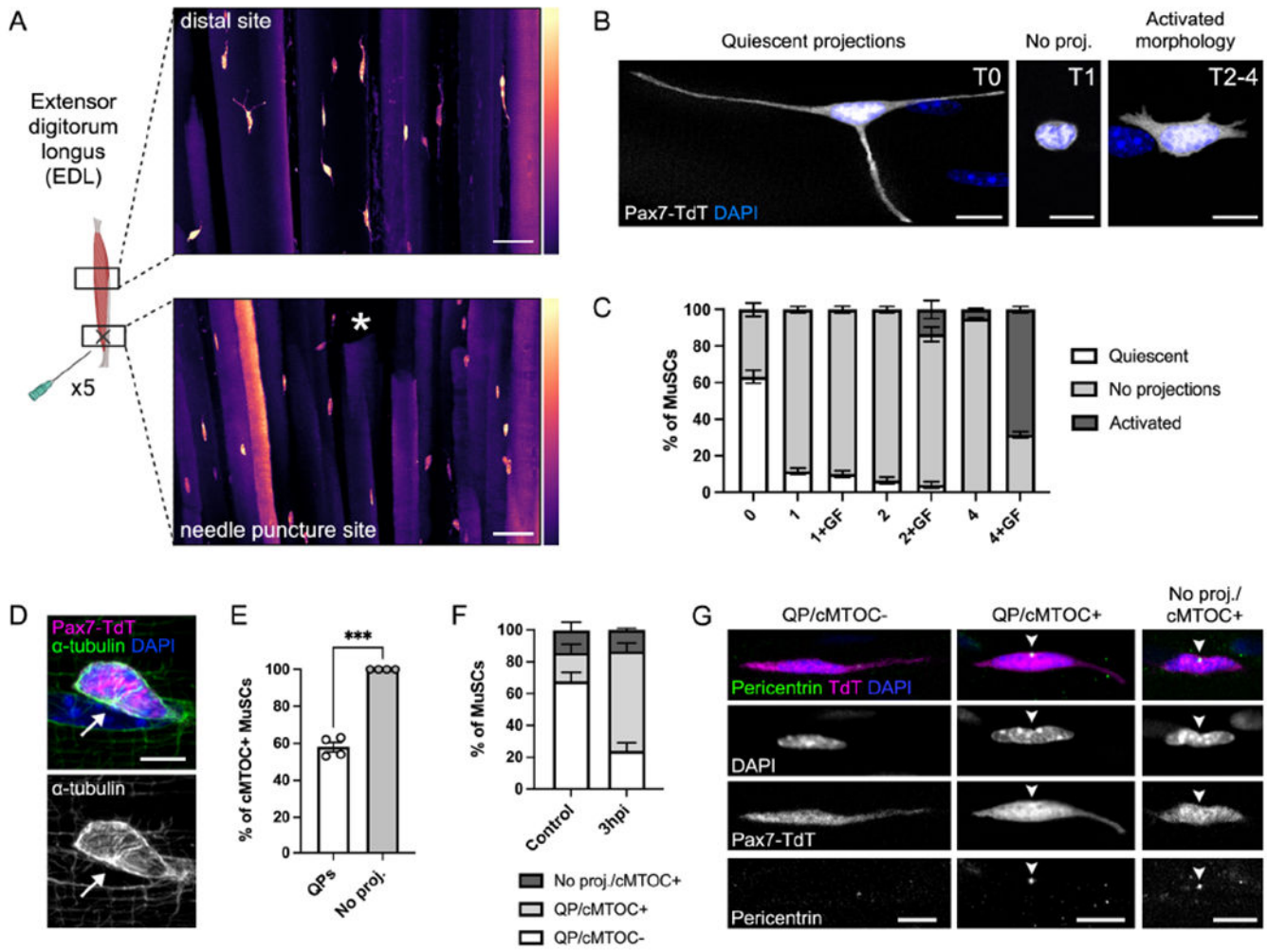

Figure 2. Retraction of quiescent projections is an early activation response.

(A) Cleared EDL muscle from Pax7-TdT mice showing MuSCs 3 hours after needle puncture injury. Asterisk indicates site of injury. LUTs indicate signal intensity. **(B-C)** Images (B) and quantification (C) of MuSC morphology over a 4-hour time course ± growth factors (GF). **(D)** Immunofluorescence of α-tubulin showing the presence of a centrosomal microtubule organizing center (cMTOC, arrow). **(E-F)** Quantification of cMTOC formation in MuSCs ± QPs on myofibers (E) or in perfusion-fixed EDL bundles from control and 3 hours post-$BaCl_2$ injury (3hpi) mice (F). **(G)** Immunofluorescence images showing pericentrin+ cMTOC formation (arrowheads) in perfusion-fixed muscle. Data represent n=3-4 mice and show mean ± s.e.m. Comparison by paired t-test (E); ***=p<0.001. Scale bars: (A) 50μm, (B,D,G) 10μm. See also Figure S2.

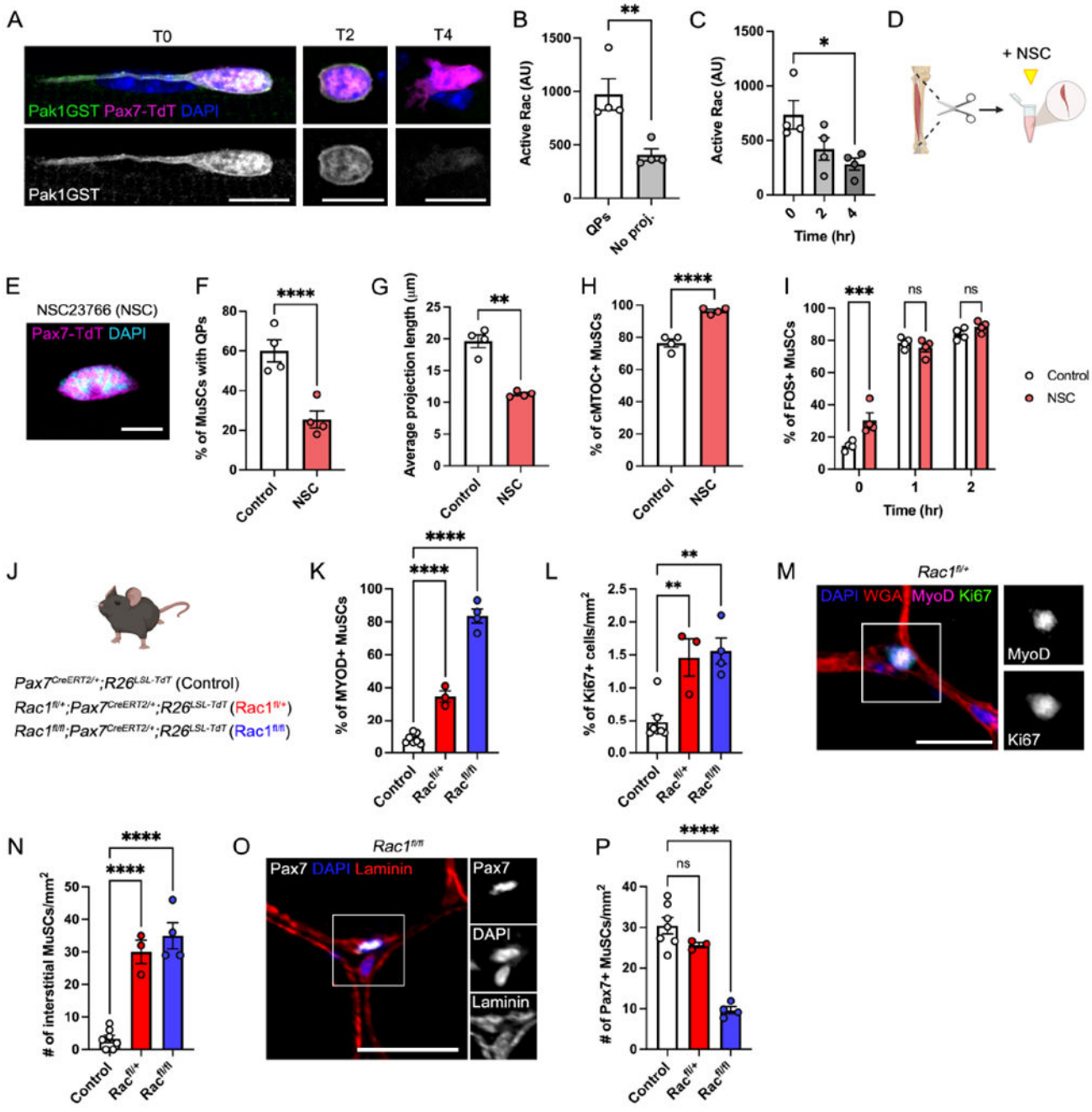

Figure 3. Rac1 maintains MuSC quiescence and is downregulated upon activation.

(A-C) Images (A) and quantification (B-C) of *in situ* assays for Rac/Cdc42 activity in T0 MuSCs ± QPs (B) or over 4 hours (C). Pak1GST binds to GTP-bound Rac/Cdc42. **(D)** Schematic showing NSC23766 (NSC) treatment during preparation of single myofibers. **(E)** Image of an NSC-treated T0 MuSC. **(F-I)** Quantification of control vs NSC-treated MuSCs showing: the frequency (F) and average length (G) of QPs, cMTOC formation at T0 (H), and the percentage of FOS+ MuSCs from T0-T2 (I). Control data are shared with Fig. 4 and Fig. S4. **(J)** Schematic showing mouse lines used for panels K-P. **(K-L)**

Quantifications of the percentage of MYOD+ MuSCs (K) and Ki67+ cells/mm^2 (L). **(M)** Image of a MYOD/Ki67+ MuSC in *Rac1*$^{fl/+}$ muscle. **(N-O)** Quantification (N) and image (O) of interstitial cells/mm^2. **(P)** Quantification of Pax7+ MuSCs/mm^2. Data represent *n*=3-4 mice and show mean ± s.e.m. Control data (A-C, F-H) are shared with Fig. 4 and S4, see Methods. Comparisons by paired *t*-test (B), one-way ANOVA with Bonferroni's multiple comparisons test (C,F-G,K-L,M,O), or two-way ANOVA with Šídák's multiple comparisons test (I); *= p<0.05, **= p<0.01, ***=p<0.001, ****=p<0.0001. Scale bars: (A) 10μm; (E) 5μm; (M,O) 25μm. See also Figure S3.

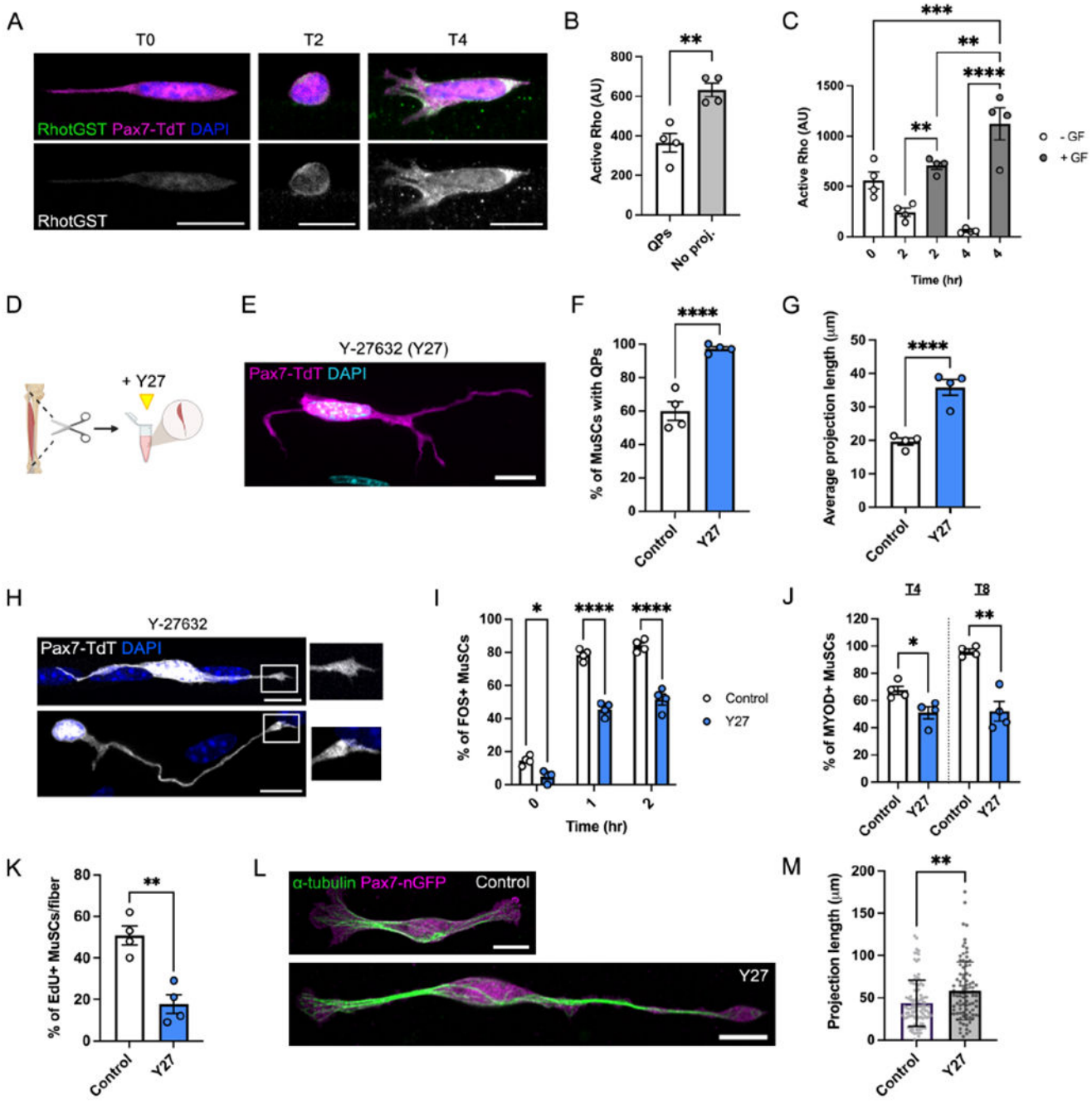

Figure 4. Rho/ROCK activity facilitates projection retraction and MuSC activation.

(A-C) Images (A) and quantifications (B-C) of *in situ* assays for Rho activity in T0 MuSCs ± QPs (B) or over 4 hours in the presence or absence of growth factors (GF) (C). RhotGST binds to GTP-bound Rho. **(D)** Schematic showing Y-27632 (Y27) treatment during preparation of single myofibers. **(E)** Image of a Y27-treated T0 MuSC. **(F-G)** Quantification of control vs. Y27-treated myofibers showing the frequency (F) and average length (G) of QPs. **(H)** Images of filopodia at the tips of Y27-treated MuSCs. **(I-L)** Quantification of control vs. Y27-treated MuSCs showing: the percentage of FOS+ cells

from T0-T2 (I), the percentage of MYOD+ cells at T4 and T8 (J), and the percentage of EdU+ cells at T30 (K). **(L-M)** Images (L) and projection lengths (M) of isolated *Pax7-nGFP* MuSCs cultured on hydrogels ± Y27. Data represent n=3-4 mice and show mean ± s.e.m. (B-C, F-G, I-K) or mean ± s.d. (M). Control data (A-C, F-J) are shared with Fig. 3 and S3, see Methods. Comparisons by paired *t*-test (B,M), one-way ANOVA with Bonferroni's multiple comparisons test (C,F-G,J-K), two-way ANOVA with Šídák's multiple comparisons test (I), or unpaired *t* test (K); *= p<0.05, **= p<0.01, ***=p<0.001, ****=p<0.0001. Scale bars: 10μm. See also Figure S4.

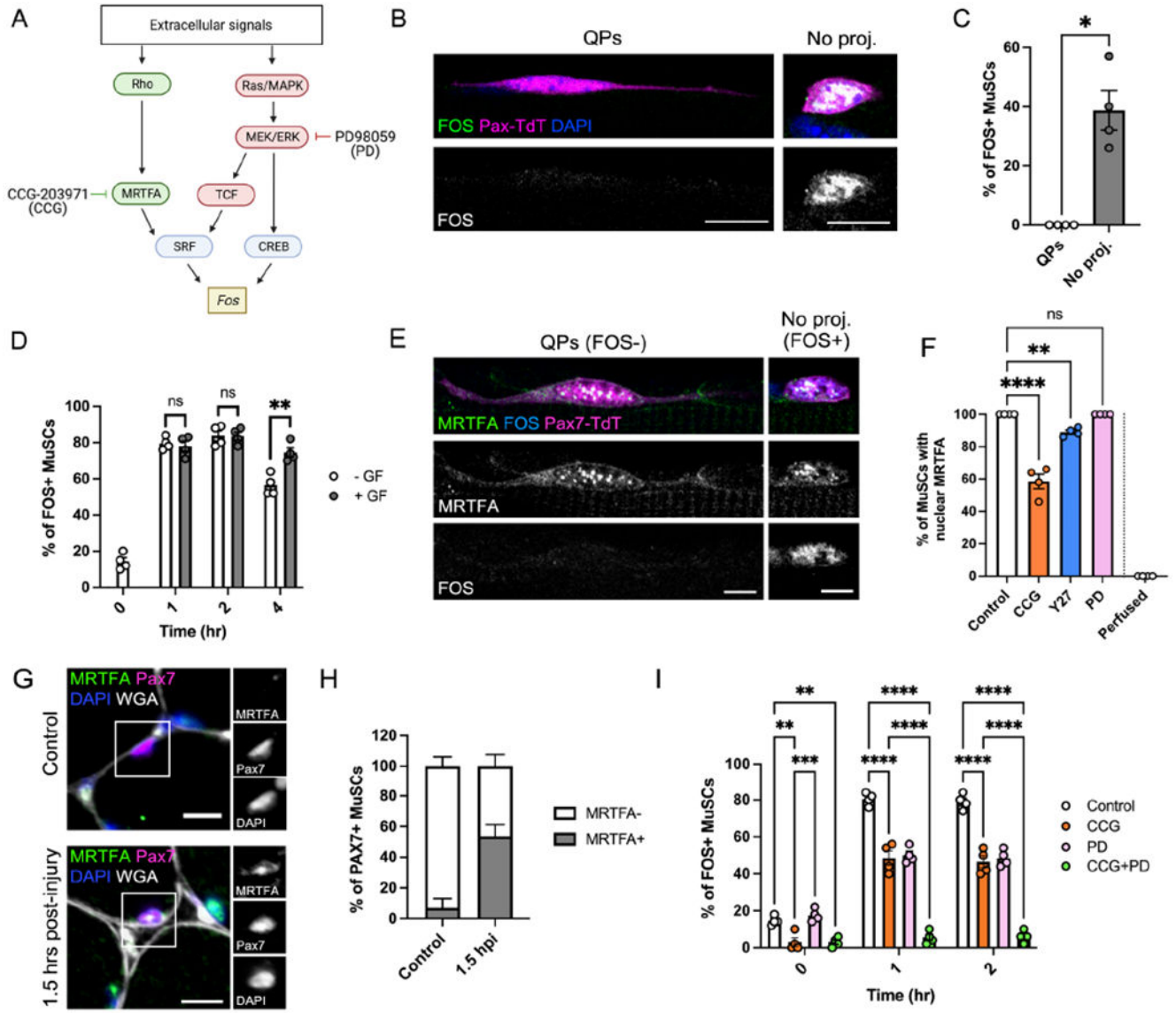

Figure 5. Rho signaling initiates FOS transcription through MRTFA.

(A) Schematic demonstrating pathways of FOS induction. CCG-203971 (CCG) inhibits MRTFA, and PD98059 (PD) inhibits MEK1/2, a critical enzyme that transduces the Ras/TCF and Ras/CREB pathways. **(B-D)** Images (B) and quantification of FOS expression in T0 MuSCs ± QPs (C) or T0-T2 MuSCs ± growth factors (GF) (D). **(E)** Image of MRTFA and FOS immunofluorescence in T0 MuSCs ± QPs. **(F)** Quantification of the percentage of T0 MuSCs with nuclear MRTFA in control, CCG, Y27, PD, and perfusion-fixed conditions. **(G-H)** Immunofluorescence images (G) and quantification (H) of the percentage of MuSCs with nuclear MRTFA in control muscle vs. 1.5 hours post-BaCl2 injury (1.5 hpi). **(I)** Quantification of FOS+ MuSCs from T0-T2 in control, CCG, PD, and CCG+PD conditions. Data represent n=4 mice and show mean ± s.e.m. Comparisons by unpaired t test with Welsh's correction (C), two-way ANOVA with Tukey's multiple comparisons test (D,I), or one-way ANOVA with Bonferroni's multiple comparisons test (F); ns= not significant, *=

p<0.05, **= p<0.01, ***=p<0.001, ****=p<0.0001. Scale bars: (B,G) 10μm, (E) 5μm. See also Figure S5.

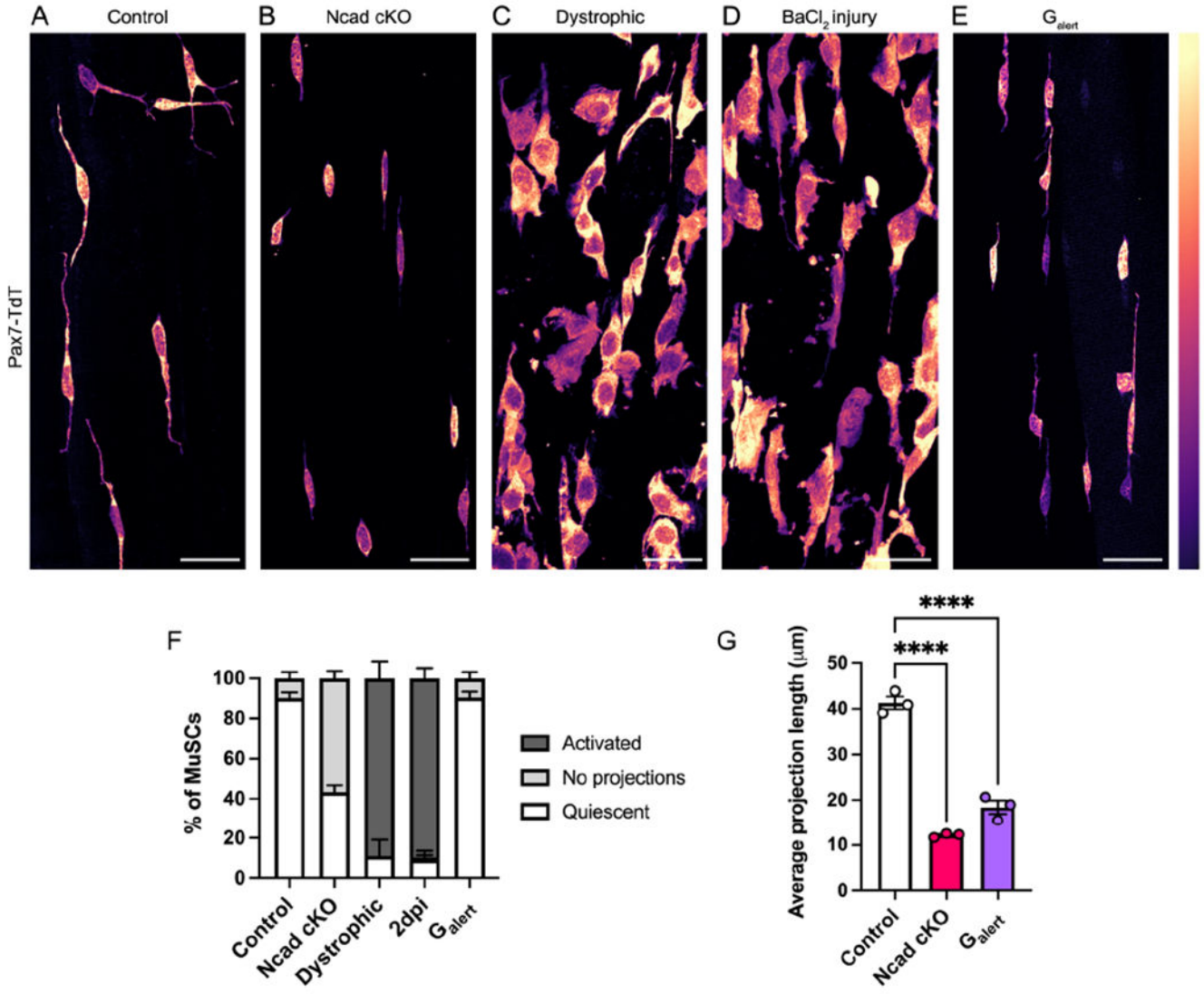

Figure 6. Projection dynamics are a conserved feature of muscle stem cell activation.

(A-E) Images of cleared EDL muscles from control (A), *Cdh2*$^{fl/fl}$;*Pax7*^{CreERT2} (Ncad cKO) (B), *Dmd*$^{mdx-4cv}$ (dystrophic) (C), 2 days post-$BaCl_2$ injury (D), and G_{alert} (E) mice. **(F-G)** Quantifications of MuSC morphology across activation conditions (F) or average QP length (G). Data represent n=3 mice and show mean ± s.e.m.. Comparisons by one-way ANOVA with Bonferroni's multiple comparisons test; ****=p<0.0001. Scale bars: 25μm.

KEY RESOURCES TABLE

REAGENT or RESOURCE	SOURCE	IDENTIFIER
Antibodies		
mouse anti-FOS	Santa Cruz Biotechnology	Cat# sc-166940; RRID:AB_10609634
Rabbit anti-α-tubulin	Abcam	Cat# ab18251; RRID:AB_2210057
Rat anti-α-tubulin	Abcam	Cat# ab6161; RRID:AB_305329
Rabbit anti-α-tubulin	GeneTex	Cat# GTX628802; RRID:AB_2716636
Mouse anti-γ-tubulin	Abcam	Cat# ab11316; RRID:AB_297920
Mouse anti-MYOD	BD Biosciences	Cat# 554130; RRID:AB_395255
Rabbit anti-Ddx6	Bethyl Laboratories	Cat# A300-461A; RRID:AB_2277216
Rabbit anti-MKL1	ProteinTech	Cat# 21166-1-AP; RRID:AB_2878822
Mouse anti-pericentrin	BD Biosciences	Cat# 611814; RRID:AB_399294
Rabbit anti-Lamin B1	Abcam	Cat# ab16048; RRID:AB_10107828
Mouse anti-N-cadherin	Santa Cruz Biotechnology	Cat# sc-8424; RRID:AB_626778
Mouse anti-Arp3	Sigma-Aldrich	Cat# A5979; RRID:AB_476749
Mouse anti-dystrophin	Santa Cruz Biotechnology	Cat# sc-73592; RRID:AB_1122390
Mouse anti-β-catenin	BD Biosciences	Cat# 610154; RRID:AB_397555
Rabbit anti-α-catenin	ProteinTech	Cat# 13974-1-AP; RRID:AB_2088078
Mouse anti-M-cadherin	Santa Cruz Biotechnology	Cat# sc-81471; RRID:AB_2077111
Mouse anti-p120ctn	BD Biosciences	Cat# 610133; RRID:AB_397536
Mouse anti-Rac1	BD Biosciences	Cat# 610650; RRID:AB_397977
Mouse Alexa Fluor 647 preconjugated Mouse anti-Ncad antibody	Santa Cruz Biotechnology	Cat# sc-8424 AF647; RRID:AB_626778
Mouse anti-Pax7-c	Developmental Studies Hybridoma Bank	Cat# PAX7; RRID:AB_2299243
Rabbit anti-Laminin	Sigma-Aldrich	Cat# L9393; RRID:AB_477163
Rabbit anti-Ki67	Abcam	Cat# ab15580; RRID:AB_443209
Hoescht	Cell Signaling Technology	Cat# 4082; RRID:AB_10626776
Wheat Germ Agglutinin, Alexa Fluor 488 Conjugate	Invitrogen	Cat# W11261
Anti-glutathione S-transferase, Alexa 488 conjugate	Thermo Fisher Scientific	Cat# A-11131; RRID:AB_2534137
Goat anti-mouse IgG1 cross-adsorbed secondary antibody, Alexa Fluor 647	Thermo Fisher Scientific	Cat# A-21240; RRID:AB_2535809
Goat anti-rabbit IgG (H+L) cross-adsorbed secondary antibody, Alexa Fluor 488	Thermo Fisher Scientific	Cat# A-11008; RRID:AB_143165
Goat anti-rabbit IgG (H+L) highly cross-adsorbed secondary antibody, Alexa Fluor 647	Thermo Fisher Scientific	Cat# A-21245; RRID:AB_2535813
Goat anti-mouse IgG2b cross-adsorbed secondary antibody, Alexa Fluor 488	Thermo Fisher Scientific	Cat# A-21141; RRID:AB_2535778
Goat anti-rat IgG2a secondary antibody, FITC	Thermo Fisher Scientific	Cat# PA1-84761; RRID:AB_933936
Goat anti-mCherry antibody	SICGEN	Cat# AB0081-500; RRID:AB_2333095
Alexa Fluor 568-conjugated Donkey anti-Goat antibody	Invitrogen	Cat# A-11057; RRID:AB_2534104
Chicken anti-GFP antibody	Novus	Cat# NB100-1614; RRID:AB_10001164

REAGENT or RESOURCE	SOURCE	IDENTIFIER
Goat anti-mouse IgG (H+L) cross-adsorbed secondary antibody, Alexa Fluor 546	Thermo Fisher Scientific	Cat# A-11003; RRID:AB_2534071
Goat anti-chicken IgY (H+L) secondary antibody, Alexa Fluor 488	Thermo Fisher Scientific	Cat# A-11039; RRID:AB_2534096
Mounting medium with DAPI	Abcam	Cat# ab104139
Chemicals, peptides, and recombinant proteins		
Tamoxifen	Sigma-Aldrich	Cat# T5648
Barium Chloride	Sigma-Aldrich	Cat# 342920
Collagenase Type I	Gibco	Cat# 17100-017
Chick embryo extract	United States Biological Corporation	Cat# NC1202490
ROCK inhibitor – Y-27632	StemCell Technologies	Cat# 72304
Myosin II inhibitor – Blebbistatin	Sigma-Aldrich	Cat# B0560
Rac inhibitor – NSC23766 trihydrochloride	Sigma-Aldrich	Cat# SML0952
Rho/MRTF/SRF inhibitor – CCG-203971	Sigma-Aldrich	Cat# SML1422
MEK1/2 inhibitor – PD 0325901	Sigma-Aldrich	Cat# PZ0162
Rhotekin-RBD protein	Cytoskeleton, Inc	Cat# RT01
Pak1-PBD protein	Cytoskeleton, Inc	Cat# PAK01
Histodenz buffer	Cosmo Bio USA	Cat# AXS-1002424
Laminin	Roche	Cat# 11243217001
Critical Commercial Assays		
Satellite Cell Isolation Kit	Miltenyi Biotec	Cat# 130-104-268
Anti-Integrin α-7 MicroBeads	Miltenyi Biotec	Cat# 130-104-261
Experimental models: Organisms/strains		
Mouse *Pax7*^{CreERT2}	IMSR	Cat# JAX:017763; RRID:IMSR_JAX:017763
Mouse *ROSA26*$^{LSL\text{-}TdTomato}$	IMSR	Cat# JAX:007914; RRID:IMSR_JAX:007914
Mouse *Rac1*$^{fl/fl}$	IMSR	Cat# JAX:005550; RRID:IMSR_JAX:005550
Mouse *Cdh2*$^{fl/fl}$	IMSR	IMSR Cat# JAX:007611, RRID:IMSR_JAX:007611
Mouse *Dmd*$^{mdx\text{-}4cv}$	IMSR	Cat# JAX:001801; RRID:IMSR_JAX:001801
Mouse *Tg:Pax7*^{nGFP}	From corresponding lab	Sambasivan et al., 2009
Software and algorithms		
Fiji	Open Source	RRID:SCR_002285; http://fiji.sc
Leica Application Suite	Licensed Software	RRID:SCR_016555; https://www.leica-microsystems.com/products/microscope-software/details/product/leica-application-suite/
GraphPad Prism	Licensed Software	RRID:SCR_002798; http://www.graphpad.com/
CellProfiler Image Analysis Software	Open Source	RRID:SCR_007358; http://cellprofiler.org